arXiv:2303.16881v1 [astro-ph.EP] 29 Mar 2023

Systematic KMTNet Planetary Anomaly Search. IX. Complete Sample of 2016 Prime-Field Planets

IN-GU SHIN,[1] JENNIFER C. YEE,[1] WEICHENG ZANG,[1,2] HONGJING YANG,[2] KYU-HA HWANG,[3] CHEONGHO HAN,[4]
ANDREW GOULD,[5,6] ANDRZEJ UDALSKI,[7] IAN A. BOND[8]

(LEADING AUTHORS),

MICHAEL D. ALBROW,[9] SUN-JU CHUNG,[3] YOUN KIL JUNG,[3,10] YOON-HYUN RYU,[3] YOSSI SHVARTZVALD,[11]
SANG-MOK CHA,[3,12] DONG-JIN KIM,[3] SEUNG-LEE KIM,[3] CHUNG-UK LEE,[3] DONG-JOO LEE,[3] YONGSEOK LEE,[3,12]
BYEONG-GON PARK,[3] RICHARD W. POGGE[6]

(THE KMTNET COLLABORATION),

PRZEMEK MRÓZ,[7] MICHAŁ K. SZYMAŃSKI,[7] JAN SKOWRON,[7] RADOSŁAW POLESKI,[7] IGOR SOSZYŃSKI,[7]
PAWEŁ PIETRUKOWICZ,[7] SZYMON KOZŁOWSKI,[7] KRZYSZTOF A. RYBICKI,[7,11] PATRYK IWANEK,[7] KRZYSZTOF ULACZYK,[13]
MARCIN WRONA,[7] MARIUSZ GROMADZKI[7]

(THE OGLE COLLABORATION)

FUMIO ABE,[14] RICHARD BARRY,[15] DAVID P. BENNETT,[15,16] APARNA BHATTACHARYA,[15,16] HIROSANE FUJII,[14]
AKIHIKO FUKUI,[17,18] RYUSEI HAMADA,[19] YUKI HIRAO,[19] STELA ISHITANI SILVA,[20,15] YOSHITAKA ITOW,[14]
RINTARO KIRIKAWA,[19] IONA KONDO,[19] NAOKI KOSHIMOTO,[21] YUTAKA MATSUBARA,[14] SHOTA MIYAZAKI,[19]
YASUSHI MURAKI,[14] GREG OLMSCHENK,[15] CLÉMENT RANC,[22] NICHOLAS J. RATTENBURY,[23] YUKI SATOH,[19]
TAKAHIRO SUMI,[19] DAISUKE SUZUKI,[19] MIO TOMOYOSHI,[19] PAUL . J. TRISTRAM,[24] AIKATERINI VANDOROU,[15,16]
HIBIKI YAMA,[19] KANSUKE YAMASHITA[19]

(THE MOA COLLABORATION)

[1] Center for Astrophysics | Harvard & Smithsonian 60 Garden St., Cambridge, MA 02138, USA
[2] Department of Astronomy, Tsinghua University, Beijing 100084, China
[3] Korea Astronomy and Space Science Institute, Daejon 34055, Republic of Korea
[4] Department of Physics, Chungbuk National University, Cheongju 28644, Republic of Korea
[5] Max Planck Institute for Astronomy, Königstuhl 17, D-69117 Heidelberg, Germany
[6] Department of Astronomy, The Ohio State University, 140 W. 18th Ave., Columbus, OH 43210, USA
[7] Astronomical Observatory, University of Warsaw, Al. Ujazdowskie 4, 00-478 Warszawa, Poland
[8] Institute of Natural and Mathematical Sciences, Massey University, Auckland 0745, New Zealand
[9] University of Canterbury, Department of Physics and Astronomy, Private Bag 4800, Christchurch 8020, New Zealand
[10] University of Science and Technology, Korea, (UST), 217 Gajeong-ro, Yuseong-gu, Daejeon 34113, Republic of Korea
[11] Department of Particle Physics and Astrophysics, Weizmann Institute of Science, Rehovot 76100, Israel
[12] School of Space Research, Kyung Hee University, Yongin, Kyeonggi 17104, Republic of Korea
[13] Department of Physics, University of Warwick, Gibbet Hill Road, Coventry, CV4 7AL, UK
[14] Institute for Space-Earth Environmental Research, Nagoya University, Nagoya 464-8601, Japan
[15] Code 667, NASA Goddard Space Flight Center, Greenbelt, MD 20771, USA
[16] Department of Astronomy, University of Maryland, College Park, MD 20742, USA
[17] Department of Earth and Planetary Science, Graduate School of Science, The University of Tokyo, 7-3-1 Hongo, Bunkyo-ku, Tokyo 113-0033, Japan
[18] Instituto de Astrofísica de Canarias, Vía Láctea s/n, E-38205 La Laguna, Tenerife, Spain
[19] Department of Earth and Space Science, Graduate School of Science, Osaka University, Toyonaka, Osaka 560-0043, Japan
[20] Department of Physics, The Catholic University of America, Washington, DC 20064, USA
[21] Department of Astronomy, Graduate School of Science, The University of Tokyo, 7-3-1 Hongo, Bunkyo-ku, Tokyo 113-0033, Japan
[22] Sorbonne Université, CNRS, UMR 7095, Institut d'Astrophysique de Paris, 98 bis bd Arago, 75014 Paris, France
[23] Department of Physics, University of Auckland, Private Bag 92019, Auckland, New Zealand
[24] University of Canterbury Mt. John Observatory, P.O. Box 56, Lake Tekapo 8770, New Zealand

ABSTRACT

As a part of the "Systematic KMTNet Planetary Anomaly Search" series, we report five new planets (namely, OGLE-2016-BLG-1635Lb, MOA-2016-BLG-532Lb, KMT-2016-BLG-0625Lb, OGLE-2016-

BLG-1850Lb, and KMT-2016-BLG-1751Lb) and one planet candidate (KMT-2016-BLG-1855), which were found by searching 2016 KMTNet prime fields. These *buried* planets show a wide range of masses from Earth–class to Super–Jupiter–class, and are located in both the disk and the bulge. The ultimate goal of this series is to build a complete planet sample. Because our work provides a complementary sample to other planet detection methods, which have different detection sensitivities, our complete sample will help us to obtain a better understanding of planet demographics in our Galaxy.

1. INTRODUCTION

To build a complete microlensing planet sample, we conduct a series of works called "Systematic KMTNet Planetary Anomaly Search" based on a large microlensing survey archive obtained by the Korea Microlensing Telescope Network (KMTNet: Kim et al. 2016). We identify planet–like anomalies using the "AnomalyFinder" algorithm (Zang et al. 2021, 2022a) instead of a traditional "by–eye" method, which can systematically identify almost all candidates showing anomalies on the light curve[1]. However, to reveal the origin of the anomaly requires (preliminary) models including possible degenerate solutions to figure out the mass ratio of the lens component (i.e., q). Also, it requires investigating the data for the anomaly to check whether or not the anomaly is caused by a false–positive signal. Thus, detailed analyses for all anomalous events found by the AnomalyFinder require significant resources and human efforts.

Hence, for the KMTNet data obtained from 2016 to 2021, we conduct the work separately for each bulge season and for observing fields with different cadences, which are divided into the prime fields (high cadence: $\Gamma = 2.0$–$4.0\,\mathrm{hr}^{-1}$) and sub–prime fields (low cadence: $\Gamma = 0.2$–$1.0\,\mathrm{hr}^{-1}$). The KMTNet field information is described in Kim et al. (2018). We have already done the systematic searches for the 2018 prime field (Wang et al. 2022; Hwang et al. 2022; Gould et al. 2022), 2018 sub–prime fields (Jung et al. 2022), 2019 prime fields (Zang et al. 2021; Hwang et al. 2022; Zang et al. 2022a), and 2019 sub–prime fields (Jung et al. 2023). In addition, Zang et al. (2023) present a complete sample of planets with the mass ratio $q < 10^{-4}$ discovered from all candidate events observed from 2016 to 2019.

This is the 9th work to build the complete sample, which is conducted for the 2016 prime–fields (i.e., BLG01, BLG41, BLG02, BLG42, BLG03, BLG43). The AnomalyFinder algorithm and candidate review identified 106 anomalous events (plus 14 events that were already published). Based on visual inspection and/or preliminary modeling, 79 were eliminated as binaries. For the remaining 13 new candidates with at least one solution with $q < 0.06$, we re-reduce the photometry to check for/remove the systematics in the data sets. Based on further analysis with the best quality data sets, 7 were eliminated because they had no reliable planetary solutions (i.e., $q < 0.03$) with $\Delta\chi^2 < 10.0$. We also investigate one additional 2016 prime–field event for the detailed analysis, which was identified using "by-eye" method and reported as a planet-like event, but was not in the final AnomalyFinder candidate list (see Appendix B). Then, we find 5 new planets and one planet candidate based on detailed analyses, which are OGLE-2016-BLG-1635Lb, MOA-2016-BLG-532Lb, KMT-2016-BLG-0625Lb, OGLE-2016-BLG-1850Lb, KMT-2016-BLG-1751Lb, and KMT-2016-BLG-1855. We note that these planetary systems are designated by the survey projects that first announced the events as is traditional, even though the planetary systems were discovered based on the systematic search using the KMTNet data archive. We describe observations of each survey in Section 2. Then, we describe the light curve analysis for the planet candidates in Section 3. We note that, for the 9 non–planetary events, we report the analysis results in Appendix A for the record. In Section 4, we present analyses for color-magnitude diagrams of the 5 planetary events. In Section 5, we present properties of the planetary systems determined based on the Bayesian analyses. Lastly, we summarize the results of this work in Section 6.

2. OBSERVATIONS

In Tables 1 and 2 (see Appendix A), we present observational information for the anomalous events, which have at least one solution with $q < 0.06$ found from preliminary modeling. For the anomalous events, we gather all available data taken from microlensing surveys for preliminary modeling. The KMTNet pipeline data are available from the KMTNet Alert System (Kim et al. 2018, https://kmtnet.kasi.re.kr/~ulens/). They were obtained using three identical 1.6 m telescopes equipped with wide–field (4 square degree) cameras. The telescopes are located at the Cerro Tololo Inter-American Observatory in Chile (KMTC), the South African Astronomical Observatory in South Africa

---

[1] Although the AnomalyFinder (AF) detects anomalies using criteria optimized to the KMTNet data, some anomalous events can be omitted because the criteria are not perfect, yet. For example, AF missed KMT-2021-BLG-2294Lb (Shin et al. 2023). Thus, the "by–eye" method can help us to improve the criteria and understand the completeness of the final planet sample.

(KMTS), and the Siding Spring Observatory in Australia (KMTA), which are in well–separated time zones to achieve near–continuous observations. Thus, the "prime–fields" of the KMTNet have high–cadences ($\Gamma \geq 2\,\mathrm{hr}^{-1}$) in I–band (Johnson–Cousins $BVRI$ filter system). Also, for the KMTC observations, KMTNet regularly takes one observation in V–band for every 10th I–band observation. We note that, for the KMTS observations, it takes one V–band observation for every 20th I–band observation.

The OGLE (Optical Gravitational Lensing Experiment: Udalski 2003; Udalski et al. 2015) data are available from the OGLE Early Warning System (Udalski et al. 1994, http://ogle.astrouw.edu.pl/ogle4/ews/ews.html) and were obtained using the 1.3 m Warsaw telescope with a $1.4\,\mathrm{deg}^2$ camera located at Las Campanas Observatory in Chile. The OGLE observations were mainly made in I band. Also, they periodically observe in V band.

The MOA (Microlensing Observations in Astrophysics: Bond et al. 2001; Sumi et al. 2003) data are available on their alert system website (http://www.massey.ac.nz/~iabond/moa/alerts/), and were obtained using a 1.8 m telescope located at Mt. John University Observatory in New Zealand. The MOA observations were taken using the MOA–Red filter (hereafter, referred to R band), which is roughly the sum of the Cousins R and I bands (wavelength ranges: 609–1109 nm, transmission ranges: 0.0–0.978).

The data of each survey were reduced by their own pipelines (KMTNet: Albrow et al. 2009, OGLE: Wozniak 2000, and MOA: Bond et al. 2001), which adopt/modify the difference image analysis technique (Tomaney & Crotts 1996; Alard & Lupton 1998). We note that, for planet-like events listed in Tables 1 and 2, the KMTNet data are re-reduced using an optimized version of pySIS (Yang et al. in prep) to obtain the best quality of data sets (hereafter, "TLC (tender loving care)" reductions) for the analyses. Also, we reduce V–band data to determine the source color using the pyDIA package (Albrow 2017; Bramich et al. 2013). We also note that some events require re-reduced data obtained from the OGLE and MOA surveys for the detailed analyses. For the KMT-2016-BLG-1751 and KMT-2016-BLG-0374 events, MOA did not alert these events. However, the events are located in the MOA fields. Therefore, the MOA team provided re-reduced data for these two events. OGLE-2016-BLG-1850 has a long baseline extending to 2017 season. The OGLE team provided re-reduced data for this event including the long baseline.

3. LIGHT CURVE ANALYSIS

3.1. *Basics of the Analysis*

We conduct detailed analysis for 13 candidates with re-reduced data sets using the optimized pySIS package (Yang et al. in prep). The analysis of the 5 planetary events and one planet candidate is presented in this section and remaining 7 events are briefly presented in Appendix A. We follow the methodology of the light curve analysis described in Shin et al. (2023). We briefly describe the analysis process, which consists of two steps, to present terminology used in this work.

First, we conduct a grid search to find all possible solutions, in particular, local minima having planetary mass ratios (i.e., $q \lesssim 0.03$). For the grid search, we start from the static 2L1S case, i.e., without motions of the lenses or source (STD), where $nLmS$ indicates number of lenses (n) and sources (m), respectively. To describe a microlensing light curve, the STD model requires seven parameters: $(t_0, u_0, t_\mathrm{E}, s, q, \alpha, \rho_*)$, which are respectively defined as the time at the peak of the light curve, impact parameter, Einstein timescale, projected separation between binary lens components in units of the angular Einstein radius (θ_E), mass ratio of the lens components (i.e., $q \equiv M_\mathrm{secondary}/M_\mathrm{primary}$), angle between the source trajectory and binary axis, and angular source radius (θ_*) scaled by θ_E (i.e., $\rho_* \equiv \theta_*/\theta_\mathrm{E}$). We set (s, q) as grid parameters for the grid search, which are most sensitive to describe anomalies on the light curve. The ranges of (s, q) are $\log_{10}(s) \in [-1.0, 1.0]$ and $\log_{10}(q) \in [-5.5, 1.0]$ with 100 grid points for each range. For five remaining parameters, we optimize them using χ^2 minimizing method called the Markov Chain Monte Carlo (MCMC) algorithm (Doran & Müller 2004). We note that α is treated as a semi-grid parameter because it is also sensitive to describing the anomalies: we start 21 seeds for α parameter within the range of $\alpha \in [0, 2\pi]$.

Second, once we find all plausible models, we refine model parameters for all cases by allowing all parameters can be freely vary within physically possible ranges. During this second process, we re–scale the errors of the data sets based on the best–fit model to make each data point contribute $\chi^2 \sim 1.0$. The error re–scaling procedure is described in Yee et al. (2012). Briefly, $e_\mathrm{R} = k\sqrt{e_\mathrm{O}^2 + e_\mathrm{S}^2}$ where e_R is re–scaled error, k is the re-scaling factor, e_O is original error, and e_S is systematics term.

Based on the STD models, we consider higher–order effects if the solutions have a high chance to detect the effects. Specifically, we firstly consider the annual microlens parallax (APRX) effect (Gould 1992) if the models show relatively long timescale (i.e., $t_\mathrm{E} \gtrsim 15$ days at least). Once we find the APRX effect, we also consider the lens–orbital (OBT)

effect because the OBT may affect the APRX measurements. Lastly, in the cases of the APRX effect detected, we test the "xallarap" effect (which is spelled backward of "parallax": Griest & Hu 1992; Han & Gould 1997; Paczynski 1997; Poindexter et al. 2005), which reflects the accelerating orbital motion of secondary source without brightness contribution of the secondary source. Because the xallarap effect can mimic the APRX effect, the xallarap test is required to confirm the APRX measurements.

From the detailed analysis, we claim the detection of planetary systems if the fiducial solutions satisfy both detection criteria: (1) the solution(s) should have $q \lesssim 0.03$ and (2) the solution(s) should have $\Delta\chi^2 \lesssim 10$ compared to other non–planetary solution(s).

Lastly, we note that, to indicate the degenerate solutions that we found, we follow the unified notation of the $s^\dagger$ formalism described in Hwang et al. (2022) and Ryu et al. (2022). Also, we can check our solutions using the formalism for validation. Here, we briefly present the $s^\dagger$ formalism for the description of each event in the following sections.

The separations ($s_\pm^\dagger$) caused by major and minor images (Gould & Loeb 1992) are expected as

$$s_\pm^\dagger \equiv \frac{\sqrt{u_{\mathrm{anom}}^2 + 4} \pm u_{\mathrm{anom}}}{2}, \tag{1}$$

where $u_{\mathrm{anom}} = (\tau_{\mathrm{anom}}^2 + u_0^2)^{1/2}$ is the offset of the source position from the host obtained from the scaled time offset from the peak of the light curve, $\tau_{\mathrm{anom}} \equiv (t_{\mathrm{anom}} - t_0)/t_{\mathrm{E}}$. The expected $s_\pm^\dagger$ can be compared to the empirical results. The comparison depends on the type of anomaly shape and the number of solutions. In general, the "bump"–shaped anomaly caused by the major image perturbation should correspond to the $s_+^\dagger$ expectation, while the "dip"–shaped anomaly caused by the minor image perturbation should correspond to the $s_-^\dagger$ expectation. For the number of solutions (i.e., degenerate cases), if we have unique solution, the empirical s should correspond to one of $s_\pm^\dagger$. If we have two degenerate solutions such as $s_\pm$, the empirical solutions have a relation of

$$s^\dagger = \sqrt{s_+ s_-}, \tag{2}$$

which should correspond to one of $s_\pm^\dagger$ values. The α can be also predicted as

$$\tan\alpha = \frac{u_0}{\tau_{\mathrm{anom}}}. \tag{3}$$

More specifically, $\alpha = \tan^{-1}(u_0/\tau_{\mathrm{anom}}) + j\pi$, where $j = (0, 1)$ for (major, minor) images, and where the range of $\tan^{-1}$ is defined as $[0, \pi]$. We note that the α expectation depends on the coordinate system of the modeling. Lastly, in the case of the dip–shaped anomaly, we can obtain the first order approximation of the q values. That is,

$$q = \left(\frac{\Delta t_{\mathrm{dip}}}{4t_{\mathrm{E}}}\right)^2 \frac{s\sin^2\alpha}{u_{\mathrm{anom}}} = \left(\frac{\Delta t_{\mathrm{dip}}}{4t_{\mathrm{E}}}\right)^2 \frac{s}{|u_0|}|\sin^3\alpha|. \tag{4}$$

We note that the predicted q generally matches the empirical q value within a factor of ~ 2. This expectation is useful for judging how valuable an event is to conduct a detailed analysis (i.e., whether or not it is a planetary event), even if the expectation could not be very accurate. The theoretical origins of the heuristic analysis and such degeneracies are described in Gaudi & Gould (1997), Griest & Safizadeh (1998), and Zhang & Gaudi (2022).

3.2. OGLE-2016-BLG-1635

The light curve of OGLE-2016-BLG-1635 (which we identified as KMT-2016-BLG-0269) exhibits a bump-shaped anomaly at $\mathrm{HJD}' = 7624.6$. In Figure 1, we present the light curve with degenerate (i.e., $s_\pm$) models. We also present the model parameters in Table 3. From a heuristic analysis, we find $\tau_{\mathrm{anom}} = 0.023$ and $u_{\mathrm{anom}} = 0.036$ based on $t_{\mathrm{anom}} = 7624.60$, $t_0 = 7624.12$, $u_0 = 0.028$, and $t_{\mathrm{E}} = 21$ days. As a result, we expect $s_-^\dagger = 0.98$ and $s_+^\dagger = 1.02$. The $s_-^\dagger$ is consistent with $s^\dagger = 0.99$ for our solutions. Although degenerate solutions exist, the mass ratios of both cases are less than 0.03, which implies that the companion is a planet by our formal definition.

The timescale of this event is about 21 days, which implies that there is a possibility of measuring the APRX considering the empirical criterion $t_{\mathrm{E}} \gtrsim 15$ days. Thus, we test the APRX models for this event. We find χ^2 improvements $\Delta\chi^2 = 7.24$ and $\Delta\chi^2 = 9.96$ for the s_- and s_+ cases, respectively. The $\Delta\chi^2$ values are too small to claim the APRX detection. Moreover, the APRX parameters are not converged for the s_- case. For the s_+ case, the

APRX model favors values of $|\pi_E| > 10$ that are not reliable because they are caused by over fitting systematics at the baseline. Hence, we conclude that the STD models should be the fiducial solutions for OGLE-2016-BLG-1635. We can only measure the upper limits of ρ_* (i.e., 3σ ranges) because the source does not cross the caustic as shown in Figure 1.

3.3. MOA-2016-BLG-532

In Figure 2, we present the light curve of MOA-2016-BLG-532 (which we identified as KMT-2016-BLG-0506), which shows a clear deviation from the 1L1S model with a finite source. Although the anomaly is neither obviously bump–shaped nor dip–shaped, we find that the heuristic analysis is valid. It yields $\tau_{\rm anom} = -0.032$ and $u_{\rm anom} = 0.034$ from $t_{\rm anom} = 7636.20$ and $t_E = 21$ days. Then, we expect $s_+^\dagger = 1.017$, which matches exactly with $s^\dagger = 1.017$ (derived from the modeling). The light curve can be well described by a 2L1S interpretation with both planet and binary cases (see light curves and geometries in Figure 2). In Table 4, we present the best-fit parameters. However, we find that the binary case shows worse fits by $\Delta\chi^2 = 20.62$ and 22.32 for the s_+ and s_- cases, respectively. The $\Delta\chi^2$ amounts are larger than our criterion to claim the planet detection. Although we conclude that this event is caused by a planetary lens system, we report both cases because the crucial part of the light curve (HJD$'$ = 7637.1–7637.4) for clearly distinguishing between planet and binary solutions is not covered.

For this event, ρ_* is measured. The signal of the finite source effect comes from the peak of the light curve, which cannot be properly described by the 1L1S interpretation (see the residual of Figure 2). The peak part can be described by 2L1S solutions (planet cases) by *touching* the cusp of the central caustic (see Figure 2). As a result, ρ_* is well measured.

We also test the APRX effect because of relatively long timescale of the event (i.e., $t_E \sim 21$ days). We find that the χ^2 improvements of $\Delta\chi^2 = 21.57$ and $\Delta\chi^2 = 12.73$ for the s_+ and s_- cases, respectively. However, the APRX fits show values too big for both cases, i.e., $|\pi_{E,N}| > 10$, which comes from over fitting systematics at the baseline. This fact implies that the APRX measurement is not reliable. Thus, we do not adopt the results of the APRX models.

3.4. KMT-2016-BLG-0625

As shown in Figure 4, the light curve of KMT-2016-BLG-0625 shows a clear bump-shaped anomaly at HJD$'$ $\sim$ 7662.95. Based on the heuristic analysis, we find $\tau_{\rm anom} = 0.609$ and $u_{\rm anom} = 0.613$ from $t_{\rm anom} = 7662.95$ and $t_E = 11.5$ days. Then, we can expect that $s_-^\dagger = 0.739$ and $s_+^\dagger = 1.352$, which are consistent with $s_- = 0.741$ and $s_+ = 1.367$, respectively, among the solutions presented in Table 5. Also, we expect $\alpha = 0.12$ or 3.26 radians, which are consistent with $\alpha = 0.12$ and 3.22 of the s_+ and s_- cases, respectively.

As shown in Table 5, we find four planetary solutions ($s_\pm$ and $s'_\pm$) that can explain the anomaly. Because of the gaps near the anomaly, the $\Delta\chi^2$ values between the models (i.e., $\Delta\chi^2 = 0.98$–3.30) are too small to distinguish between them, although the model light curves show quite different features caused by the different caustic geometries presented in Figure 4. Although we cannot break the degeneracy of the planetary solutions, all cases indicate the companion of the lens system is a planet, i.e., $q = \mathcal{O}(10^{-4})$ (see Table 5).

As shown in Figure 4, all planetary solutions produce the anomaly by crossing the caustic(s). As a result, we can measure the ρ_* despite the non-optimal coverage. We do not test for the APRX measurement because of the relatively short timescale (i.e., $t_E \sim 11$ days).

Because the bump-type planetary anomaly can often lead to a 2L1S/1L2S degeneracy (Gaudi 1998), we check the 1L2S case for this event. In Table 5, we present the best-fit model of the 1L2S interpretation. We find that the 1L2S case is disfavored by $\Delta\chi^2 = 7.35$. However, the $\Delta\chi^2$ amount is not enough to conclusively resolve the 2L1S/1L2S degeneracy. Nevertheless, because we measure the ρ_* of the secondary source, we can measure the lens–source relative proper motion of the secondary source ($\mu_{\rm rel,S_2}$) to check the 1L2S model. We find (see Section 4) that $\mu_{\rm rel,S_2} = 0.83 \pm 0.22 \,{\rm mas\,yr^{-1}}$. By comparison, Gould (2022) found that for observed microlensing events with planetary-type anomalies, low proper motions have probabilities

$$p(\leq \mu_{\rm rel}) = \frac{(\mu_{\rm rel}/2\sigma_\mu)^{\nu+1}}{[(\nu+1)/2]!} \to \frac{\mu_{\rm rel}^2}{4\sigma_\mu^2} \to 2.8 \times 10^{-2} \left(\frac{\mu_{\rm rel}}{1\,{\rm mas\,yr^{-1}}}\right)^2, \tag{5}$$

where $\sigma_\mu = 3\,{\rm mas\,yr^{-1}}$ and $\nu = 1$. See also Equation (9) of Jung et al. (2023). Applying this formula to the 1L2S solution, we find $p = 1.9\%$. This would, in itself, be a reasonably strong argument against the 1L2S solution. When combined with the fact that this solution is disfavored by $\Delta\chi^2 = 7.35$, we consider it to be decisive. Therefore, we

reject the 1L2S solution and conclude that KMT-2016-BLG-0625 is caused by a planetary lens system. However, we note that the mass ratio q varies by a factor ~ 3 over the four degenerate solutions.

3.5. *OGLE-2016-BLG-1850*

The light curve of OGLE-2016-BLG-1850 (which we identified as KMT-2016-BLG-1307) shows a dip–shaped anomaly at HJD$' \sim 7663$. Based on the heuristic analysis, we can expect $s_-^\dagger = 0.812$ and $q = 0.9 \times 10^{-4}$ (based on $\tau_{\text{anom}} = 0.126$ and $u_{\text{anom}} = 0.419$ that are found from $t_{\text{anom}} = 7663.15$ and $t_{\text{E}} = 63.0$ days), which corresponds well with the empirical values: $s^\dagger = 0.813$ and $q \sim 1.0 \times 10^{-4}$.

In Figure 5, we present the observed light curve with zoom–ins of the anomaly. We also present the best-fit model light curves of the STD and APRX cases shown in Table 6. We find that both STD models (i.e., inner and outer cases) can describe the planetary anomaly as shown in Figure 6. However, the STD cases show a very long timescale ($t_{\text{E}} \sim 210$ days), which implies that the light curve is likely to be affected by a strong APRX effect. As expected, we find that the STD model cannot properly describe the 2017 baseline. Thus, we consider the ARPX effect. Then, we find a substantial χ^2 improvement of $\Delta\chi^2 \gtrsim 100$, which mostly comes from the better fit of 2017 baseline (see Figure 5). Also, all APRX solutions can well describe the planetary anomaly as shown in Figure 6. In Figure 7, we present caustic geometries of all cases for comparison. We note that OGLE-2016-BLG-1850 is a non–caustic–crossing event. As a result, we cannot precisely measure ρ_* (only upper limits are available).

In Figure 8, we present the distributions of the APRX measurements, which are well converged. However, tests are required before we conclude that the APRX models should be the fiducial solutions for this event. First, because the lens–orbital motion can affect the APRX measurements (especially, the uncertainty of the APRX measurement), we test the lens–orbital effect (OBT). We conduct OBT+APRX models for each APRX case. We find that the OBT+APRX models show negligible χ^2 improvements, which are $\Delta\chi^2 \lesssim 0.5$ for the inner cases and $\Delta\chi^2 \lesssim 3.0$ for the outer cases, respectively. We also find that there is no effect on the uncertainties of the APRX measurements.

Second, to check the APRX models, we add xallarap to the models by introducing five parameters, which are North and East components of the xallarap vector ($\xi_{\text{E},N}$, $\xi_{\text{E},E}$), the phase angle (ϕ), the inclination of the orbit (i), and orbital period (P). We find that xallarap cases show χ^2 improvements of $\Delta\chi^2 = 17.0$–22.1 compared to the APRX cases, which are marginal $\Delta\chi^2$ amounts to firmly claim the xallarap models can be fiducial solutions for this event. Moreover, although the best–fit model favors $\log_{10}(P) = 0.2$ as shown in Figure 9, we find that the xallarap models at $\log_{10}(P) = 0.0$ show $\Delta\chi^2 \lesssim 6.0$ compared to the best–fit xallarap model of each case. The clues imply that the asymmetry of the light curve is due to the APRX effect rather than xallarap effect. Thus, we conclude that the fiducial solutions for this event are the APRX models.

3.6. *KMT-2016-BLG-1751*

In Figure 10, we present the observed light curve of KMT-2016-BLG-1751, which shows a clear planetary anomaly (i.e., dip–feature) at the peak of the light curve. Based on the heuristic analysis ($\tau_{\text{anom}} \sim 0.00$ and $u_{\text{anom}} = 0.11$ from $t_{\text{anom}} = 7501.00$ and $t_{\text{E}} = 10.0$ days), we expect $s_-^\dagger = 0.946$, which is well matched to both $s^\dagger = \sqrt{s_- s_+} = 0.944$ and $s^\dagger = \sqrt{s'_- s'_+} = 0.947$. We also expect $q \simeq 0.003$ (for both $s^\dagger$ cases), which agrees with the q values presented in Table 7 to within a factor of ~ 2.

We find that several solutions can explain the anomaly because the coverage of the anomaly (HJD$' = 7500.8$–7502.4) is non-optimal. Thus, despite including MOA data, the gap in the anomaly produces degenerate solutions. In Table 7, we present model parameters of the solutions. In Figures 11 and 12, we also present the s–q parameter space with the locations of each solution and their caustic geometries. The competing solutions show relatively small $\Delta\chi^2$ values compared to the best-fit solution (i.e., s_+ case): 8.53, 5.70, 8.78, and 10.78 for s'_+, s_-, s'_-, and s''_- cases, respectively. For the $s_\pm$ and $s'_\pm$ case, we obtain a best-fit value for ρ_*. However, as might be expected from the geometries, we find that the measurements are consistent with zero at 3σ. Thus, in these cases, we effectively have only an upper limit on ρ_*, so we will apply a ρ_* weight function in the Bayesian analysis in Section 5. For the s''_- case, ρ_* is measured from the caustic–crossing. However, the s''_- solution does not satisfy our χ^2 criterion (i.e., $\Delta\chi^2 < 10.0$). Thus, we remove the s''_- case from our fiducial solutions for determining lens properties of this event. However, because the $\Delta\chi^2$ of this case is very close to the χ^2 criterion, we present parameters and figures of this solution for completeness. Lastly, because of the short timescale (i.e., $t_{\text{E}} \sim 10$ days), we do not conduct the APRX modeling for this event.

3.7. *KMT-2016-BLG-1855*

In Figure 13, we present the observed light curve of KMT-2016-BLG-1855 with the best–fit model curve and caustic geometry. The observed light curve exhibits anomalies at the peak. We find that the anomaly can be described by a source approaching a diamond–shaped central caustic, which is in the regime of a Chang & Refsdal lens (C–R: Chang & Refsdal 1979). The best–fit model shows $\frac{1}{q} = 0.023 \pm 0.012$ which satisfies our mass ratio criterion to claim planet detection. However, we find that there exist possible solutions caused by the close/wide degeneracy (Griest & Safizadeh 1998), the offset degeneracy (Zhang & Gaudi 2022; Zhang et al. 2022), and 2L1S/1L2S degeneracy (Gaudi 1998). We also check for the α–degeneracy (i.e., degeneracy caused by the angle of source trajectory), which can occur for C–R lenses. These solutions are denoted $n(\pi/2)$, where $n = (1, 2, 3)$. In Tables 8 and 9, we present model parameters of the best–fit and degenerate models. In Figures 14 and 15, we present all possible solutions with their caustic geometries and residuals for comparison.

We find total 7 degenerate solutions including the 1L2S case. For the 2L1S cases, we find the initial parameters of A, B, C, and D solutions based on the grid search. We also find initial parameters for their paired offset-degeneracy solutions (i.e., A′, B′, C′, and D′) using heuristic analysis: $s' = (s^{\dagger}_{\pm})^2 / s_{\pm}$ where subscripts $+$ and $-$ indicates the $s > 1$ and $s < 1$ cases, respectively. Note that we transform our coordinates system from "secondary" to "primary" components to conduct the heuristic analysis because the analysis is valid for the "primary" coordinates system. Then, we refine the model parameters to check the degeneracy (note that we restore the coordinates for direct comparison).

For the A and A′ pair, the heuristic analysis predicts $s' = 3.680$. The paired offset-degeneracy solution of the A case (i.e., A′) is consistent with the $3(\pi/2)$ C–R case, which has an empirical value of $s = 3.780 \pm 0.088$. This A family degeneracy can be resolved (see below). For the B and B′ pair, the heuristic analysis predicts $s' = 3.600$, which is consistent with the empirical $s = 3.708 \pm 0.121$ from the B′ case. This B family is a C–R lensing case, which shows large uncertainties in the set of $(t_{\rm E}, s, q)$ parameters. For the C and C′ pair, the heuristic analysis predicts $s' = 1.162$, which is consistent with the empirical value of $s = 1.161 \pm 0.042$ from the C′ case. Indeed, the C family is caused by close/wide degeneracy. For the D case, the heuristic analysis expects $s' = 2.951$. However, we find that the paired offset solution evolves toward the B case. Indeed, the caustic geometry of the D case is asymmetric, which is different from the C–R lens case. Thus, because the source trajectory is not perpendicular the binary axis, the paired solution from the heuristic analysis cannot describe the peak of the light curve, and we would not necessarily expect it to (Gaudi & Gould 1997). In all cases, the ρ_* measurements are uncertain and give only upper limits of ρ_* values as expected from non–crossing caustic geometries.

All the 2L1S models nominally have long timescales ($t_{\rm E}$), but they also have $q > 1.0$ (i.e., they approach the secondary, less-massive, lens component). For these cases, the actual timescale ($t'_{\rm E}$) of the event should be scaled by $t'_{\rm E} = t_{\rm E}\sqrt{q}$ as shown in Tables 8 and 9. Hence, given that $t'_{\rm E} \sim 15$ days, it is not surprising that we do not detect the APRX effect (i.e., $\Delta\chi^2_{\rm STD-APRX} = 2.7$). Thus, we conclude that the STD models are the fiducial solutions for this event.

As shown in Figures 14 and 15, all cases describe the peak anomaly well. Although they nominally have $\Delta\chi^2 > 10$ compared to the best–fit case, we find that χ^2 differences mostly come from the baseline part (HJD′ > 7600). The best-fit case has a wide caustic, which creates a very shallow bump peaking at HJD′ ~ 7717, $\Delta I \sim 0.01$ magnitudes above the baseline observations (see the blue dashed line). However, systematics may exist in the baseline data at this level, especially considering the dispersion of the baseline data (i.e., $\Delta I \sim 0.65$ magnitudes). Thus, we compute $\Delta\chi^2$ without the baseline data of HJD′ > 7600 (which $t_0+ \sim 1.5\,t_{\rm E} \sim 7595.25$) because the χ^2 contributions at the baseline cannot be considered reliable. After this cut, the $\Delta\chi^2$ values for all cases (except the A′ case) are less than 9 as shown in Tables 8 and 9. Hence, we cannot claim to resolve most degenerate solutions.

The 1L2S model is completely degenerate with the 2L1S models and cannot be excluded based on physical considerations. First, the finite source effect is not measured; the ρ_* distributions of both sources reach zero within 3σ. Moreover, because of the severe extinction ($A_I = 5.97$; Gonzalez et al. 2012), additional information to conclusively resolve the degeneracy, such as the source color (see Section 4), is not available for this event.

Thus, we treat KMT-2016-BLG-1855 as a planet candidate, and we strongly counsel against cataloging it as a "planet".

4. CMD ANALYSIS

For the five planetary events, we measure the angular source radius (θ_*) using the conventional method described in Yoo et al. (2004), i.e., the color-magnitude diagram (CMD) analysis. The θ_* measurement is important. If we measure

ρ_* from the finite–source effect, we can determine $\theta_{\rm E} = \theta_*/\rho_*$. Furthermore, even if we cannot measure the ρ_*, θ_* is required to apply the ρ_* distributions as constraints on the Bayesian analysis.

We proceed with this analysis based on multi–band observations (I– and V–bands) taken from KMTNet survey (i.e., KMTC). We align the KMTNet instrumental color and magnitudes to the OGLE–III scales using cross–matching of field stars. We note that the position of the red giant clump centroid (RGC) is determined based on the OGLE–III CMD (Szymański et al. 2011). In Figure 16, we present CMDs of the five planetary events for the best–fit cases with the positions of RGC, source, and blend. We also present all information from the CMD analysis, including θ_*, $\theta_{\rm E}$ and $\mu_{\rm rel}$, in Table 10. We note that the intrinsic color of the RGC is adopted from Bensby et al. (2011). The de-reddened magnitude of the RGC is adopted from Nataf et al. (2013). The de-reddened colors and magnitudes of source and blend are determined by assuming they experienced same amount of stellar extinction of the RGC. Lastly, we determine the θ_* using the surface brightness–color relation adopted from Kervella et al. (2004).

Note that we proceed differently for the special case of the putative second source in the 1L2S solution for KMT-2016-BLG-0625. We find $I_{\rm S,0} = 19.345 \pm 0.010$ using the method of Yoo et al. (2004). Then, we derive $I_{\rm S_2,0} = 25.112 \pm 0.231$ based on the $q_{\rm flux}$ value of the 1L2S model. We convert the de-reddened I–band magnitude of the second source to absolute I–band magnitude (M_I) for the second source by adopting $M_{I,\rm RGC} = -0.12 \pm 0.09$ and $I_{\rm RGC,0} = 14.335$ from Nataf et al. (2013): $M_{I,\rm S_2} = 10.656 \pm 0.248$. We can estimate the radius of the second source, $R_{\rm S_2} \sim 0.208\,R_\odot$, based on studies for stellar properties (Pecaut et al. 2012; Pecaut & Mamajek 2013). Thus, we find the angular radius of the second source is $\theta_{*,\rm S_2} \sim 0.128\,\mu$as, which yields $\mu_{\rm rel,S_2} = 0.83 \pm 0.22\,{\rm mas\,yr^{-1}}$. Note that we adopt the distance to the second source ($D_{\rm S_2} \sim 7.59\,{\rm kpc}$) from Nataf et al. (2013).

For KMT-2016-BLG-1855, the field is highly extincted ($A_I = 5.97$; Gonzalez et al. 2012), so is not possible to measure the source color in V-band from the KMTNet data. We construct an I-H CMD for this event by cross-matching the OGLE-III catalog (Szymański et al. 2011) to VVV DR2 (Minniti et al. 2017), and we convert the KMT pyDIA I magnitude of the source to the OGLE-III system. This that suggests the source is a red clump giant. However, the clump is extended in both color and magnitude in the CMD. Both the lack of a color measurement and the uncertainty in the clump magnitude would make $\theta_\star$ highly uncertain. However, there are no meaningful constraints on $\rho_\star$, so we do not calculate a value for $\theta_\star$ because it has no bearing on the analysis.

We also measure astrometric offsets between baseline objects and sources to check whether or not the blend light can be used as constraints. For all planetary events, we find that the blend is separated by $> 0.3''$, so it is dominated by a star that is not the lens.

5. PLANET PROPERTIES

5.1. *Bayesian Formalism*

To determine the lens properties, two additional observables are simultaneously required. They are the angular Einstein ring radius ($\theta_{\rm E}$) and the amplitude of the microlens parallax vector ($|\pi_{\rm E}|$), which are measured from the effects of the finite source and microlens parallax, respectively. However, the events for which both observables are simultaneously measured are relatively rare. Indeed, we can measure only one of these observables out of five planetary events presented in this work. Thus, we estimate the lens properties using the Bayesian analysis. We follow the Bayesian formalism described in Shin et al. (2023) to generate the Galactic prior. Then, we apply the measured observable as a constraint on the Galactic prior. In Table 11, we present the applied constraints and the lens properties for each event. For the notation of the constraint, $t_{\rm E}$ indicates a Gaussian weight function constructed based on the best–fit value of the $t_{\rm E}$ parameter and its uncertainty. $\theta_{\rm E}$ indicates the Gaussian weight adopted from the measured $\theta_{\rm E}$ if ρ_* is certainly measured. ρ_* indicates a weight function built based on the $\Delta\chi^2$ distribution as a function of ρ_* if the ρ_* measurement is uncertain. Lastly, $\pi_{\rm E}$ indicates a constraint using the 2D APRX distributions described in Ryu et al. (2019). In Table 11, we present various lens properties for each event because each event has degenerate solutions, which yield different lens properties. For ease of cataloging, we present "adopted" values for each property by adopting the method described in Jung et al. (2023), i.e., weighted average values.

5.2. *OGLE-2016-BLG-1635*

For the Bayesian analysis of this event, we apply constraints obtained from $t_{\rm E}$ (i.e., the Gaussian weight) and ρ_* weight functions on the Galactic prior, because the ρ_* measurements are uncertain and the APRX is not measured. Note that we can evaluate the effect of the ρ_* weight on the posterior before conducting the Bayesian analysis. If the

lower limit on the relative lens–source proper motion, $\mu_{\rm rel,+3\sigma} \equiv \theta_*/(\rho_{*,+3\sigma}t_{\rm E}) \lesssim 1\,{\rm mas\,yr^{-1}}$, the effect is minor. As expected (see the $\mu_{\rm rel}$ column of Table 10), the effects of ρ_* are minor for both solutions.

The Bayesian results indicate that the lens system of this event consists of an M dwarf host star ($M_{\rm host} \sim 0.4\,M_\odot$) and a super–Jupiter–mass planet with a mass of $M_{\rm planet} \sim 11.5\,M_{\rm J}$, which is close to the limit of planetary objects. The planet orbits the host with a projected separation $a_\perp \sim 1.31$ au or ~ 3.82 au, which is beyond its snow line. The planetary system is located in the Galactic bulge with the distance ~ 6.6 kpc from us. Hence, this event is caused by a typical microlensing planetary system, which is a giant planet orbiting an M dwarf host beyond snow line (Ida & Lin 2005; Kennedy & Kenyon 2008).

5.3. MOA-2016-BLG-532

For this event, the ρ_* values are measured. Thus, we apply $t_{\rm E}$ and $\theta_{\rm E}$ constraints on the Bayesian analyses. The lens system of this event consists of a late–type M–dwarf host star ($M_{\rm host} \sim 0.1\,M_\odot$) and a super–Neptune–mass planet ($M_{\rm planet} \sim 7.2\,M_{\rm N}$) orbiting with a projected separation, $a_\perp \sim 0.56$ au or ~ 1.36 au. The planetary system is located at the distance with $D_{\rm L} \sim 7.4$ kpc from us. Similarly to OGLE-2016-BLG-1635 this event is also caused by a typical microlensing planet.

5.4. KMT-2016-BLG-0625

Despite the non-optimal coverage, we can measure ρ_* for this event. Thus, we apply $t_{\rm E}$ and $\theta_{\rm E}$ constraints on the Bayesian analyses. For this event, The Bayesian results for the lens system spans a wide range of properties because of the degenerate solutions (i.e., due to different q and ρ_* for each solution, see Table 5). The host star is an M dwarf with the mass range of $M_{\rm host} \sim 0.2$–$0.3\,M_\odot$. For the s_- case (the best–fit solution), the planet could be a Neptune–mass planet with a mass of $M_{\rm planet} \sim 1.36\,M_{\rm N}$ orbiting the host with a projected separation of $a_\perp \sim 1.3$ au. For the remaining cases, the planet could be a super–Earth–mass planet with a mass range of $M_{\rm planet} \sim 2.0$–$9.0\,M_\oplus$ orbiting the host with a projected separation range of $a_\perp \sim 0.9$–1.9 au. The planetary system belongs to the Galactic bulge with a distance range of $D_{\rm L} \sim 6.1$–6.7 kpc.

5.5. OGLE-2016-BLG-1850

For this event, we find the APRX effect on the light curve. However, the ρ_* measurements are uncertain. Thus, we apply $t_{\rm E}$, ρ_* weights, and $\boldsymbol{\pi}_{\rm E}$ constraints on the Bayesian analyses. The $\boldsymbol{\pi}_{\rm E}$ constraints have major effects on the posteriors, while the ρ_* constraints have only minor effects as expected from $\mu_{\rm rel,+3\sigma} \lesssim 1\,{\rm mas\,yr^{-1}}$ (see Table 10).

The planetary system of this event consists of an M–dwarf host star ($M_{\rm host} \sim 0.2$–$0.3\,M_\odot$) and a super–Earth–mass planet. We find that the planet mass of the inner cases ($M_{\rm planet} \sim 9\,M_\oplus$) is smaller than those of the outer cases ($M_{\rm planet} \sim 11\,M_\oplus$). The planet orbits the host with a projected separation of $a_\perp \sim 1.4$–1.5 au beyond its snow line. The system is located at the distance of $D_{\rm L} \sim 2$ kpc from us, i.e., in the disk, which is expected by considering the strong microlens parallax effect.

5.6. KMT-2016-BLG-1751

For this event, we conduct Bayesian analyses for $s_\pm$ and $s'_\pm$ solutions by applying $t_{\rm E}$ and ρ_* weights as constraints. We find that the lens system consists of an M–dwarf host ($M_{\rm host} \sim 0.18\,M_\odot$) and a Jupiter–class planet ($M_{\rm planet} \sim 0.7$–$1.2\,M_{\rm J}$), which is located at the distance of ~ 7.05 kpc from us. The planet orbits the host with the projected separation of $a_\perp \sim 1.2$–1.4 au.

We note that, as mentioned in Section 3.6, the s''_- case is removed from our fiducial solutions. Thus, although we conduct the Bayesian analysis for this case, we do not include the lens properties of this cease in Table 11. However, for completeness, we present the lens properties of this case. The Bayesian analysis applied $t_{\rm E}$ constraint indicates that the lens system consists of a M–dwarf host star ($M_{\rm host} = 0.18^{+0.28}_{-0.11}\,M_\odot$) and a Super Neptune–mass planet ($M_{\rm planet} = 2.5^{+4.25}_{-1.57}\,M_{\rm N}$) with a projected separation of $1.28^{+0.54}_{-0.44}$ au. The system is located at the distance of $7.04^{+0.54}_{-1.38}$ kpc and the relative lens–source proper motion is $\mu_{\rm rel} = 7.56^{+3.45}_{-2.68}\,{\rm mas\,yr^{-1}}$. The results are similar to the lens properties of our fiducial solutions because the $t_{\rm E}$ value of the s''_- is similar to them, except for the planet mass, which is caused by the smallest q value of the s''_- model. On the other hand, the Bayesian analysis applying $t_{\rm E}$ and ρ_* weights shows an extreme lens system caused by the unusually small $\theta_{\rm E}$. That is, the lens system could consist of very–low mass host ($M_{\rm host} = 0.02^{+0.05}_{-0.01}\,M_\odot$ and sub Neptune–mass planet ($M_{\rm planet} = 0.31^{0.71}_{-0.19}\,M_{\rm N}$) with the projected separation of $0.31^{+0.06}_{-0.07}$. The system could be located at the distance of $8.17^{+1.05}_{-1.04}$ kpc. The relative lens–source proper motion is

$\mu_{\rm rel} = 1.59^{+0.21}_{-0.34}\,{\rm mas\,yr^{-1}}$, which is inconsistent with the typical value of bulge–lens/bulge–source microlensing event (5–$10\,{\rm mas\,yr^{-1}}$). If the lens star were resolved by future adaptive optics imaging, this could definitively rule out the s''_- solution.

6. SUMMARY

We found 5 new planetary systems and one planet candidate through a systematic anomaly search for 2016 prime–fields of the KMTNet data archive. These "buried" planets have various properties. For OGLE-2016-BLG-1635, the planetary system consists of an M dwarf host ($M_{\rm host} \sim 0.4\,M_\odot$) and a super–Jupiter–mass planet ($M_{\rm planet} \sim 11.5\,M_{\rm J}$), which orbits the host with a projected separation of 1.3 or 3.8 au. The system is located at a distance of ~ 6.6 kpc from us. For MOA-2016-BLG-532, the lens system indicates that a super–Neptune–mass planet ($M_{\rm planet} \sim 7.2\,M_{\rm N}$) orbits a late M–dwarf host star ($M_{\rm host} \sim 0.1\,M_\odot$) with a projected separation of 0.6 or 1.4 au. The planetary system is located at a distance of ~ 7.4 kpc from us. For KMT-2016-BLG-0625, because of the degenerate solutions, the planetary system consists of an M dwarf host star with mass in the range 0.1–$0.3\,M_\odot$ and a planet with mass in the range $2.0\,M_\oplus$–$1.4\,M_{\rm N}$. The system is located at a distance in the range 6.1–6.7 kpc. For OGLE-2016-BLG-1850, the planetary system consists of an M dwarf host star ($M_{\rm host} \sim 0.3\,M_\odot$) and a Super–Earth-mass planet ($M_{\rm planet} = 9$–$11\,M_\oplus$) with a projected separation of ~ 1.5 au. The system is located at a distance of 2 kpc. For KMT-2016-BLG-1751, we adopt the lens properties of $s_\pm$ and $s^\dagger_\pm$ cases, which indicate that a Jupiter–class planet ($M_{\rm planet} = 0.7$–$1.2\,M_{\rm J}$) orbits an M–dwarf host ($M_{\rm host} \sim 0.18\,M_\odot$). The system is located at a distance of ~ 7.05 kpc.

Our goal in the series including this work is to build a complete planet sample discovered by the microlensing method for the 2016–2021 KMTNet data archive. In Table 12, we present all microlensing planets discovered on the KMTNet prime fields in 2016, which are published planets that are recovered by the AnomalyFinder and five newly discovered in this work. The horizontal line separates planets expected to be part of the final statistical sample and those whose mass ratios are likely too uncertain or too large to be included.

As discussed in Clanton & Gaudi (2014a,b) and Shin et al. (2019), each planet detection method has different detection sensitivity, which provides complementary planet samples for studying planet demographics and planet frequency in our Galaxy. Our works are important for a complete microlensing planet sample. Indeed, although the sample size of microlensing planets is relatively small compared to other methods such as radial velocity and transits, the microlensing planet sample is less biased to host mass because, in principle, the microlensing method can detect any foreground objects regardless of their host brightness. Thus, a complete microlensing planet sample can help us to obtain a better understanding of planet demographics in our Galaxy.

APPENDIX

A. NON–PLANETARY EVENTS

We report on the analysis of binary–lens events, that are found by AnomalyFinder as candidate planetary events. From the initial analyses, we find that the light curves of these events could be described both binary-lens and planet-lens interpretations. However, based on analyses using TLC reductions, we find that these events disfavor planetary solutions ($q < 0.03$) by $\Delta\chi^2 > 15$. Thus, we cannot claim certain detection of the planets. In Table 2, we present observational information of these events.

A.1. *OGLE-2016-BLG-0987*

The light curve of OGLE-2016-BLG-0987 (which we identified as KMT-2016-BLG-0020) shows deviations from the 1L1S interpretation ($\Delta\chi^2_{1L1S-2L1S} = 159.68$). From the 2L1S modeling, we find several 2L1S solutions that can explain the deviations. Among the solutions, four are binary–lens cases and three are planet–lens cases. The best-fit solution is the binary–lens case with $(s, q) = (0.492 \pm 0.013, 0.108 \pm 0.005)$. However, the lowest χ^2 planetary solution $((s, q(\times 10^{-4}) = (0.702 \pm 0.081, 59.198 \pm 49.265))$ shows $\Delta\chi^2 = 26.60$ compared to the best-fit solution. The $\Delta\chi^2$ cannot satisfy our criterion to claim the planet detection. Also, the planetary solutions cannot describe the subtle bump feature at HJD$' \sim 7528$. Thus, we conclude OGLE-2016-BLG-0987 should be removed from the planet sample. We note that, although this event is not likely to be caused by a planetary lens system, the best-fit solution indicates that the companion could be a low-mass object such as a brown dwarf.

A.2. *MOA-2016-BLG-123*

For this event (which we identified as KMT-2016-BLG-0106), we find seven local solutions based on analysis using the TLC reductions. However, not all local minima satisfy our q criterion (i.e., $q < 0.03$) for claiming a planet detection. The best-fit solution indicates that the event was caused by a binary lens system, i.e., $(s, q) = (2.671 \pm 0.089, 1.113 \pm 0.099)$. Among the local minima, the model showing the lowest q value ($q = 0.052 \pm 0.003$) is disfavored by $\Delta\chi^2 = 122.70$ compared to the best-fit solution. Thus, we conclude this event should be removed from the planet sample.

A.3. *OGLE-2016-BLG-0558*

For this event (which we identified as KMT-2016-BLG-0157), we found two solutions that showed planet-like mass ratio ($q \sim 0.03$) from the initial analysis. We, therefore, refine the solutions based on the TLC reductions. The analysis using the TLC reductions clearly shows localized solutions (i.e., $s_\pm$ cases) with $(s, q) = (0.580 \pm 0.009, 0.048 \pm 0.003)$ and $(2.158 \pm 0.027, 0.057 \pm 0.003)$ for the s_- and s_+ cases, respectively. However, the mass ratios do not satisfy our criterion ($q < 0.03$) to claim the planet detection although the companion is likely to be a low–mass object such as a brown dwarf. Hence, we remove this event from the planet sample.

A.4. *KMT-2016-BLG-0374*

We find plausible solutions within the planetary regime ($q < 0.03$) from the initial analysis. However, based on the analysis using TLC reductions, we find that the best-fit solutions are binary–lens cases with $(s, q) = (6.89, 0.55)$ and $(0.20, 0.22)$ for the s_+ and s_- cases, respectively. We also find that the planet–like models are disfavored by $\Delta\chi^2 = 19.74$ and 18.60 for the s_+ and s_- cases, respectively. The planet–like solutions cannot satisfy the criterion for the planet detection. Thus, we conclude to remove this event from our planet samples.

A.5. *KMT-2016-BLG-0446*

The AnomalyFinder detects subtle a deviation on the light curve at HJD$' \sim 7631.0$–7636.0 based on the pipeline data. The anomaly can be explained by planetary models. However, the TLC reductions reveal that the anomaly is a false–positive. Then, we find that the light curve can be explained by the 1L1S interpretation rather than any 2L1S interpretations. Thus, we remove KMT-2016-BLG-0446 from our sample.

A.6. *OGLE-2016-BLG-1722*

We find that the best-fit solution of OGLE-2016-BLG-1722 (which we identified as KMT-2016-BLG-1716) is caused by a binary lens with the mass ratio, $q = 1.247 \pm 0.204$ (i.e., $q \sim 0.80$) for the s_- case (the competing s_+ solution also exists). The best–fit light curves are caused by approaching a diamond-shaped caustic. Thus, a four-fold degeneracy exists (i.e., four solutions with different source trajectories for different α values).

We also find alternative planetary solutions with the mass ratio, $q = (26.095 \pm 8.013) \times 10^{-4}$ for the s_- case. However, $\Delta\chi^2_{\text{(planet-binary)}} = 29.23$. The $\Delta\chi^2$ cannot satisfy our criterion ($\Delta\chi^2 < 10$) to claim a planet detection. Indeed, these planetary models clearly show worse fits in their residuals. Hence, we decide to remove OGLE-2016-BLG-1722 from our planet candidate sample for full analysis.

A.7. *OGLE-2016-BLG-0974*

The best-fit solutions of OGLE-2016-BLG-0974 (which we identified as KMT-2016-BLG-1863) is a binary–lens model with $(s, q) = (0.277 \pm 0.005, 0.306 \pm 0.031)$. There exists a s_+ solution, $(s, q) = (5.626 \pm 0.215, 0.782 \pm 0.133)$, with

$\Delta\chi^2 = 6.96$ caused by the close/wide degeneracy. We find that the solutions having the lowest χ^2 in the planetary regime ($q < 0.03$) are disfavored by $\Delta\chi^2 = 78.89$ and 73.52 for the $s_- : [s, q] = [0.576 \pm 0.007, (161.679 \pm 8.552) \times 10^{-4}]$ and $s_+ : [s, q] = [1.657 \pm 0.025, (176.374 \pm 10.013) \times 10^{-4}]$ cases, respectively. Thus, we conclude that OGLE-2016-BLG-0974 is caused by a binary lens system rather than a planetary lens system.

B. OGLE-2016-BLG-0185

We also present the analysis of OGLE-2016-BLG-0185, which was identified by eye as a planet candidate but not selected as anomalous in the AnomalyFinder process. We conduct a detailed analysis based on TLC reductions for this event. We find that the best–fit solution is a binary lens case with $(s, q) = (4.834 \pm 0.201, 3.480 \pm 1.110)$. This is equivalent to $\frac{1}{q} = 0.287 \pm 0.085$, which clearly implies a binary lens origin. We also search for a planetary model. The best planetary model that satisfies our mass-ratio criterion has $(s, q) = (0.724 \pm 0.037, 0.013 \pm 0.004)$, but is disfavored by $\Delta\chi^2 = 46$ compared to the best–fit model. Thus, we conclude that this event was caused by a binary lens system.

Although OGLE-2016-BLG-0185 turned out to be a binary lens event, it is still an important test case for verifying the AnomalyFinder process and assessing possible failure modes. In fact, the AnomalyFinder algorithm did identify a series of possible anomalies in this event, but the human operator rejected them as "fake." In OGLE-2016-BLG-0185, the anomaly occurs over the peak of the event, but because the event occurs early in the microlensing season, it is only sparsely covered, and the primary deviation from a point lens occurs in only the KMTA datasets. In addition, the event has a short timescale. Hence, due to the χ^2 likelihood estimation, a point lens fit is biased toward the points at the peak (which have the smallest errorbars) and the baseline points (which dominate the numbers), and so it normalized the flux levels of the KMTA data so that the peak points (due to the anomaly) lay on the point lens light curve. As a result, the "anomalies" identified by the AnomalyFinder were in the rising and falling parts of the light curve and caused by the bad flux normalization rather than the actual anomaly (see Figure 17).

OGLE-2016-BLG-0185 is qualitatively similar to KMT-2021-BLG-2294, which was also missed by the AnomalyFinder process (Shin et al. 2023). They are both short timescale events ($t_E = 10.8 \pm 1.3$ and 7.1 ± 0.3 days, respectively) and had anomalies that occurred at the peak of the events. On the other hand, the reasons the anomalies were missed are distinctly different: in OGLE-2016-BLG-0185, the wrong anomaly was identified, but in KMT-2021-BLG-2294, the anomaly did not meet the detection threshold. The latter case is acceptable from the perspective of constructing a statistical sample of events. However, the failure for OGLE-2016-BLG-0185 is more concerning, but could be compensated for by adding an additional criterion to the AnomalyFinder algorithm to check for outliers in flux normalization.

REFERENCES

Alard, C. & Lupton, R. H. 1998, ApJ, 503, 325.
  doi:10.1086/305984

Albrow, M. D., Horne, K., Bramich, D. M., et al. 2009,
  MNRAS, 397, 2099. doi:10.1111/j.1365-2966.2009.15098.x

Albrow, M. D. 2017, MichaelDAlbrow/pyDIA: Initial
  release on github, V1.0.0, Zenodo,
  doi:10.5281/zenodo.268049

Bensby, T., Adén, D., Meléndez, J., et al. 2011, A&A, 533,
  A134. doi:10.1051/0004-6361/201117059

Bond, I. A., Bennett, D. P., Sumi, T., et al. 2017, MNRAS,
  469, 2434. doi:10.1093/mnras/stx1049

Bond, I. A., Abe, F., Dodd, R. J., et al. 2001, MNRAS,
  327, 868. doi:10.1046/j.1365-8711.2001.04776.x

Bramich, D. M., Horne, K., Albrow, M. D., et al. 2013,
  MNRAS, 428, 2275, doi:10.1093/mnras/sts184

Chang, K. & Refsdal, S. 1979, Nature, 282, 561.
  doi:10.1038/282561a0

Clanton, C. & Gaudi, B. S. 2014a, ApJ, 791, 90.
  doi:10.1088/0004-637X/791/2/90

Clanton, C. & Gaudi, B. S. 2014b, ApJ, 791, 91.
  doi:10.1088/0004-637X/791/2/91

Doran, M. & Müller, C. M. 2004, JCAP, 2004, 003.
  doi:10.1088/1475-7516/2004/09/003

Gaudi, B. S. 1998, ApJ, 506, 533. doi:10.1086/306256

Gaudi, B. S. & Gould, A. 1997, ApJ, 486, 85.
  doi:10.1086/304491

Gonzalez, O. A., Rejkuba, M., Zoccali, M., et al. 2012,
  A&A, 543, A13. doi:10.1051/0004-6361/201219222

Gould, A. 1992, ApJ, 392, 442. doi:10.1086/171443

Gould, A. & Loeb, A. 1992, ApJ, 396, 104.
  doi:10.1086/171700

Gould, A., Han, C., Zang, W., et al. 2022, A&A, 664, A13.
  doi:10.1051/0004-6361/202243744

Gould, A. 2022, arXiv:2209.12501.
  doi:10.48550/arXiv.2209.12501

Gould, A., Shvartzvald, Y., Zhang, J., et al. 2023, arXiv:2303.08876. doi:10.48550/arXiv.2303.08876

Griest, K. & Safizadeh, N. 1998, ApJ, 500, 37. doi:10.1086/305729

Griest, K. & Hu, W. 1992, ApJ, 397, 362. doi:10.1086/171793

Han, C. & Gould, A. 1997, ApJ, 480, 196. doi:10.1086/303944

Han, C., Udalski, A., Gould, A., et al. 2017, AJ, 154, 223. doi:10.3847/1538-3881/aa9179

Han, C., Bond, I. A., Gould, A., et al. 2018, AJ, 156, 226. doi:10.3847/1538-3881/aae38e

Hwang, K.-H., Kim, H.-W., Kim, D.-J., et al. 2018, Journal of Korean Astronomical Society, 51, 197. doi:10.5303/JKAS.2018.51.6.197

Hwang, K.-H., Zang, W., Gould, A., et al. 2022, AJ, 163, 43. doi:10.3847/1538-3881/ac38ad

Ida, S. & Lin, D. N. C. 2005, ApJ, 626, 1045. doi:10.1086/429953

Jung, Y. K., Hwang, K.-H., Ryu, Y.-H., et al. 2018, AJ, 156, 208. doi:10.3847/1538-3881/aae319

Jung, Y. K., Zang, W., Han, C., et al. 2022, AJ, 164, 262. doi:10.3847/1538-3881/ac9c5c

Jung, Y. K., Zang, W., Wang, H., et al. 2023, in prep.

Kennedy, G. M. & Kenyon, S. J. 2008, ApJ, 673, 502. doi:10.1086/524130

Kervella, P., Thévenin, F., Di Folco, E., et al. 2004, A&A, 426, 297. doi:10.1051/0004-6361:20035930

Kim, S.-L., Lee, C.-U., Park, B.-G., et al. 2016, Journal of Korean Astronomical Society, 49, 37. doi:10.5303/JKAS.2016.49.1.037

Kim, D.-J., Kim, H.-W., Hwang, K.-H., et al. 2018, AJ, 155, 76. doi:10.3847/1538-3881/aaa47b

Koshimoto, N., Shvartzvald, Y., Bennett, D. P., et al. 2017, AJ, 154, 3. doi:10.3847/1538-3881/aa72e0

Minniti, D., Lucas, P., & VVV Team 2017, VizieR Online Data Catalog, II/348

Mróz, P., Han, C., and, et al. 2017, AJ, 153, 143. doi:10.3847/1538-3881/aa5da2

Nataf, D. M., Gould, A., Fouqué, P., et al. 2013, ApJ, 769, 88. doi:10.1088/0004-637X/769/2/88

Paczynski, B. 1997, astro-ph/9711007

Pecaut, M. J., Mamajek, E. E., & Bubar, E. J. 2012, ApJ, 746, 154. doi:10.1088/0004-637X/746/2/154

Pecaut, M. J. & Mamajek, E. E. 2013, ApJS, 208, 9. doi:10.1088/0067-0049/208/1/9

Poindexter, S., Afonso, C., Bennett, D. P., et al. 2005, ApJ, 633, 914. doi:10.1086/468182

Ryu, Y.-H., Yee, J. C., Udalski, A., et al. 2018, AJ, 155, 40. doi:10.3847/1538-3881/aa9be4

Ryu, Y.-H., Hwang, K.-H., Gould, A., et al. 2019, AJ, 158, 151. doi:10.3847/1538-3881/ab3a34

Ryu, Y.-H., Hwang, K.-H., Gould, A., et al. 2021, AJ, 162, 96. doi:10.3847/1538-3881/ac062a

Ryu, Y.-H., Kil Jung, Y., Yang, H., et al. 2022, AJ, 164, 180. doi:10.3847/1538-3881/ac8d6c

Shin, I.-G., Ryu, Y.-H., Yee, J. C., et al. 2019, AJ, 157, 146. doi:10.3847/1538-3881/ab07c2

Shin, I.-G., Yee, J. C., Gould, A., et al. 2023, AJ, 165, 8. doi:10.3847/1538-3881/ac9d93

Shvartzvald, Y., Yee, J. C., Calchi Novati, S., et al. 2017, ApJL, 840, L3. doi:10.3847/2041-8213/aa6d09

Sumi, T., Abe, F., Bond, I. A., et al. 2003, ApJ, 591, 204. doi:10.1086/375212

Szymański, M. K., Udalski, A., Soszyński, I., et al. 2011, AcA, 61, 83

Tomaney, A. B. & Crotts, A. P. S. 1996, AJ, 112, 2872. doi:10.1086/118228

Udalski, A. 2003, AcA, 53, 291

Udalski, A., Szymanski, M., Kaluzny, J., et al. 1994, AcA, 44, 227

Udalski, A., Szymański, M. K., & Szymański, G. 2015, AcA, 65, 1

Wang, H., Zang, W., Zhu, W., et al. 2022, MNRAS, 510, 1778. doi:10.1093/mnras/stab3581

Wozniak, P. R. 2000, AcA, 50, 421

Yang, H., Zhang, X., Hwang, K.-H., et al. 2020, AJ, 159, 98. doi:10.3847/1538-3881/ab660e

Yee, J. C., Shvartzvald, Y., Gal-Yam, A., et al. 2012, ApJ, 755, 102. doi:10.1088/0004-637X/755/2/102

Yoo, J., DePoy, D. L., Gal-Yam, A., et al. 2004, ApJ, 603, 139. doi:10.1086/381241

Zang, W., Hwang, K.-H., Udalski, A., et al. 2021, AJ, 162, 163. doi:10.3847/1538-3881/ac12d4

Zang, W., Yang, H., Han, C., et al. 2022a, MNRAS, 515, 928. doi:10.1093/mnras/stac1883

Zang, W., Jung, Y. K., Yang, H., et al. 2023, AJ, 165, 103. doi:10.3847/1538-3881/acb34b

Zang et al. in prep.

Zhang, K. & Gaudi, B. S. 2022, ApJL, 936, L22. doi:10.3847/2041-8213/ac8c2b

Zhang, K., Gaudi, B. S., & Bloom, J. S. 2022, Nature Astronomy, 6, 782. doi:10.1038/s41550-022-01671-6

Table 1. Observations of 2016 planetary events

Event			Location			obs. info.	
KMTNet	OGLE	MOA	R.A. (J2000)	Dec (J2000)	(ℓ, b)	A_I	Γ (hr^{-1})
0269	**1635**	$\cdots$	$17^h54^m01^s.22$	$-30°46'38''.10$	$(-0°.65, -2°.51)$	1.82	2.0
0506	1749	**532**	$17^h57^m44^s.18$	$-29°06'25''.60$	$(+1°.20, -2°.37)$	1.56	4.0
0625	$\cdots$	$\cdots$	$18^h05^m39^s.66$	$-27°13'36''.70$	$(+3°.70, -2°.96)$	0.95	4.0
1307	**1850**	$\cdots$	$17^h52^m00^s.18$	$-32°12'38''.20$	$(-2°.10, -2°.86)$	2.01	4.0
1751	$\cdots$	avail.	$17^h53^m28^s.62$	$-32°09'06''.52$	$(-1°.89, -3°.10)$	2.11	4.0
1855	$\cdots$	$\cdots$	$17^h50^m13^s.25$	$-29°12'26''.39$	$(+0°.29, -1°.00)$	5.97	4.0

Note— Boldface indicates the "discovery" name of each event.

Table 2. Observations of 2016 non–planetary events

Event			Location			obs. info.	
KMTNet	OGLE	MOA	R.A. (J2000)	Dec (J2000)	(ℓ, b)	A_I	Γ (hr^{-1})
0020	**0987**	$\cdots$	$17^h56^m34^s.37$	$-27°59'31''.99$	$(+2°.04, -1°.59)$	1.78	4.0
0106	$\cdots$	**123**	$17^h54^m17^s.90$	$-28°55'15''.74$	$(+0°.99, -1°.62)$	1.72	1.0
0157	**0558**	$\cdots$	$17^h57^m45^s.40$	$-28°20'07''.40$	$(+1°.88, -1°.98)$	1.61	4.0
0374	$\cdots$	avail.	$17^h54^m48^s.45$	$-30°59'04''.42$	$(-0°.74, -2°.76)$	1.43	4.0
0425	**0185**	$\cdots$	$17^h52^m35^s.43$	$-31°19'51''.60$	$(-1°.28, -2°.52)$	2.24	4.0
0446	$\cdots$	$\cdots$	$17^h51^m52^s.02$	$-28°50'00''.17$	$(+0°.79, -1°.12)$	3.13	4.0
0641	**0779**	$\cdots$	$18^h05^m59^s.40$	$-28°06'13''.21$	$(+2°.97, -3°.45)$	0.84	1.0
1716	**1722**	555	$17^h55^m21^s.82$	$-30°42'36''.90$	$(-0°.44, -2°.72)$	1.73	4.0
1863	**0974**	351	$18^h01^m23^s.99$	$-27°33'20''.30$	$(+2°.95, -2°.29)$	1.41	4.0

Note— Boldface indicates the "discovery" name of each event.

Table 3. Model Parameters of OGLE-2016-BLG-1635

Parameter	s_-	s_+
$\chi^2/\mathrm{N_{data}}$	$5434.309/5436$	$5442.023/5436$
t_0 [HJD$'$]	7624.124 ± 0.013	7624.118 ± 0.014
u_0	0.028 ± 0.004	0.028 ± 0.003
t_E [days]	20.908 ± 2.239	21.997 ± 2.252
s	0.587 ± 0.014	1.684 ± 0.043
q $(\times 10^{-4})$	254.587 ± 33.644	247.586 ± 30.858
$\langle \log_{10} q \rangle$	-1.594 ± 0.058	-1.620 ± 0.056
α [rad]	5.056 ± 0.028	5.047 ± 0.030
$\rho_{*,\mathrm{limit}}$	< 0.0037	< 0.0041

Note— HJD$'$ = HJD $- 2450000.0$.

Table 4. Model Parameters of MOA-2016-BLG-532

| Cases	**Planet**		Binary		
Parameter	$\mathbf{s_-}$	$\mathbf{s_+}$	Parameter	s_-	s_+
$\chi^2/\mathrm{N_{data}}$	$\mathbf{12638.981/12647}$	$\mathbf{12637.673/12647}$	$\Delta\chi^2_{\mathrm{binary-planet}}$	22.322	20.619
t_0 [HJD$'$]	$\mathbf{7636.877 \pm 0.003}$	$\mathbf{7636.885 \pm 0.003}$	t_0 [HJD$'$]	7636.934 ± 0.003	7636.938 ± 0.003
u_0	$\mathbf{0.009 \pm 0.001}$	$\mathbf{0.009 \pm 0.001}$	u_0	0.009 ± 0.001	0.007 ± 0.001
t_E [days]	$\mathbf{20.786 \pm 1.356}$	$\mathbf{20.547 \pm 1.491}$	t_E [days]	21.606 ± 1.392	25.921 ± 1.427
s	$\mathbf{0.653 \pm 0.018}$	$\mathbf{1.584 \pm 0.048}$	s	0.278 ± 0.013	4.742 ± 0.362
q $(\times 10^{-4})$	$\mathbf{40.382 \pm 5.534}$	$\mathbf{40.441 \pm 6.491}$	q	0.156 ± 0.029	0.232 ± 0.062
$\langle \log_{10} q \rangle$	$\mathbf{-2.387 \pm 0.058}$	$\mathbf{-2.403 \pm 0.070}$	$\langle \log_{10} q \rangle$	-0.765 ± 0.073	-0.595 ± 0.100
α [rad]	$\mathbf{2.938 \pm 0.008}$	$\mathbf{2.949 \pm 0.008}$	α [rad]	3.026 ± 0.010	3.036 ± 0.008
ρ_* $(\times 10^{-4})$	$\mathbf{46.956 \pm 3.995}$	$\mathbf{47.591 \pm 5.055}$	ρ_* $(\times 10^{-4})$	73.386 ± 5.591	59.520 ± 3.267

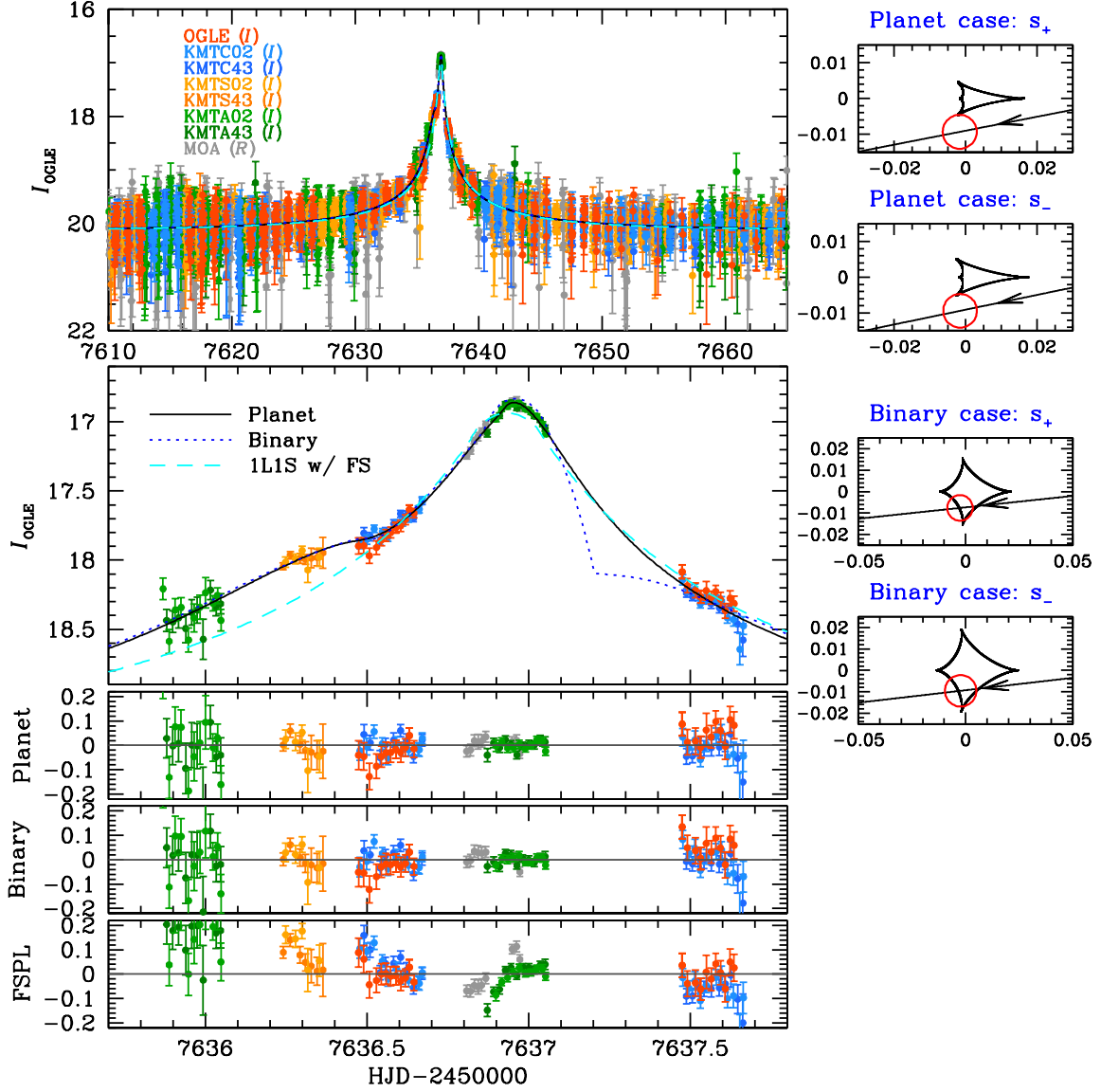Note— HJD$'$ = HJD $- 2450000.0$.
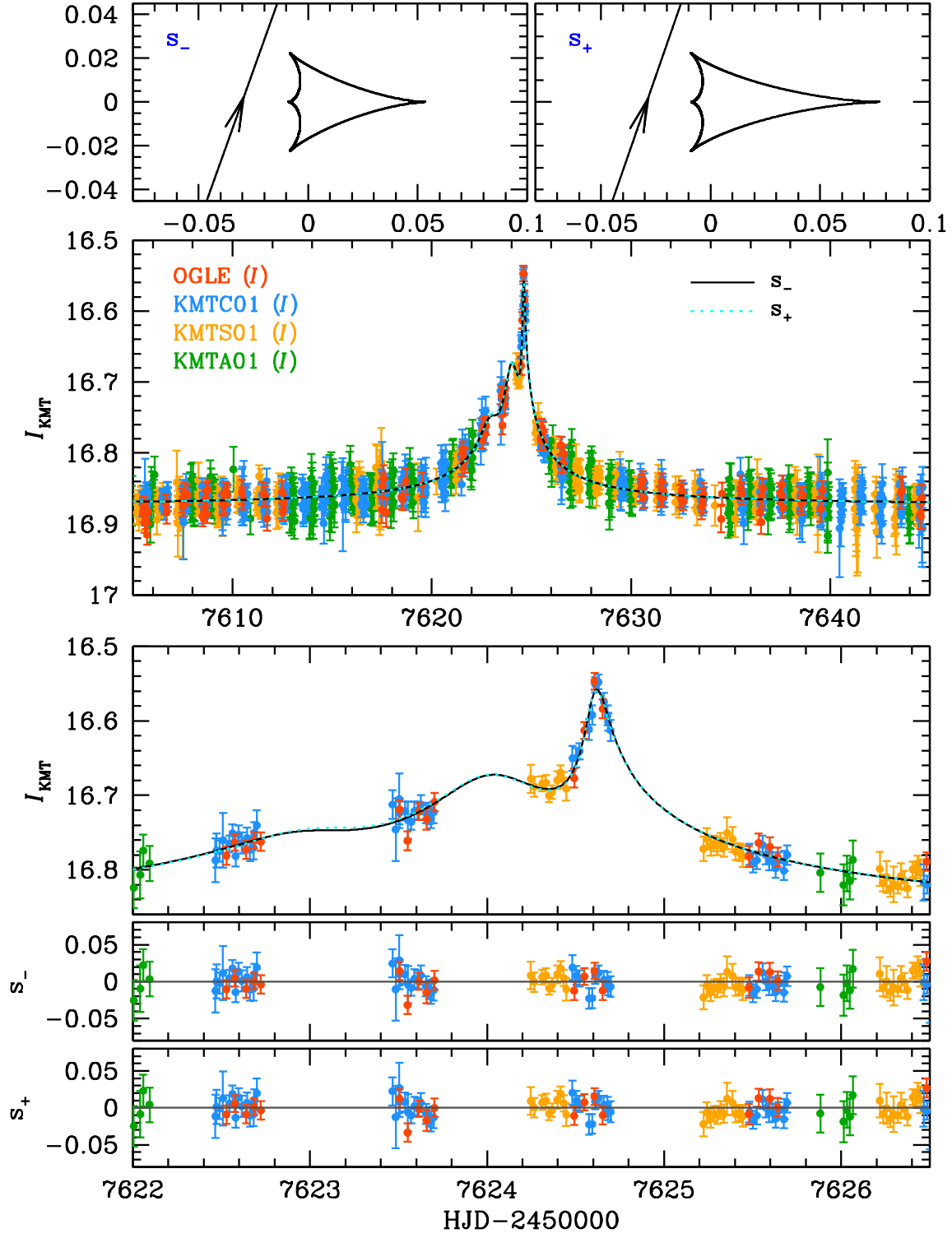
Figure 1. Light curve of OGLE-2016-BLG-1635 with $s_{\pm}$ models and their caustic geometries.

Figure 2. Light curve of MOA-2016-BLG-532 with the best-fit planetary model. We compare the planetary solution (black solid line) to binary (blue dotted line) and 1L1S with finite–source (cyan dashed line) models. We also present caustic geometries of 2L1S models on the right side for comparison.

Table 5. Model Parameters of KMT-2016-BLG-0625

Parameter	s_-	s'_-	s_+	s'_+	Parameter	1L2S
$\chi^2/\mathrm{N_{data}}$	8014.084/8021	8015.097/8021	8015.065/8021	8017.379/8021	$\chi^2/\mathrm{N_{data}}$	8021.432/8021
t_0 [HJD$'$]	7655.951 ± 0.008	7655.948 ± 0.008	7655.951 ± 0.008	7655.950 ± 0.008	t_{0,S_1} [HJD$'$]	7655.953 ± 0.008
u_0	0.073 ± 0.004	0.072 ± 0.004	0.075 ± 0.005	0.076 ± 0.004	u_{0,S_1}	0.078 ± 0.007
t_E [days]	11.494 ± 0.466	11.576 ± 0.466	11.335 ± 0.508	11.217 ± 0.405	t_E [days]	10.946 ± 0.491
s	0.741 ± 0.009	0.741 ± 0.009	1.367 ± 0.018	1.358 ± 0.015	t_{0,S_2} [HJD$'$]	7662.943 ± 0.010
q ($\times 10^{-4}$)	2.357 ± 1.123	1.793 ± 1.048	0.727 ± 0.254	0.317 ± 0.173	u_{0,S_2} ($\times 10^{-4}$)	3.751 ± 19.751
$\langle \log_{10} q \rangle$	-3.451 ± 0.130	-3.498 ± 0.136	-4.154 ± 0.159	-4.321 ± 0.159	$\cdots$	$\cdots$
α [rad]	3.217 ± 0.008	3.220 ± 0.008	0.122 ± 0.003	0.121 ± 0.002	q_flux	0.005 ± 0.001
ρ_* ($\times 10^{-4}$)	12.256 ± 6.613	20.969 ± 7.334	17.498 ± 7.796	17.656 ± 7.383	ρ_{*,S_2} ($\times 10^{-4}$)	51.309 ± 13.447

NOTE— HJD$'$ = HJD $-$ 2450000.0. We note that the ρ_{*,S_1} is not measured for the 1L2S case. The upper limit (3σ range) only can be measured: $\rho_{*,S_1} < 0.117$.

Table 6. Model Parameters of OGLE-2016-BLG-1850

	STD		APRX			
Parameter	inner	outer	inner ($u_0 > 0$)	outer ($u_0 > 0$)	inner ($u_0 < 0$)	outer ($u_0 < 0$)
$\chi^2/\mathrm{N_{data}}$	8108.940/7995	8108.800/7995	8004.449/7995	8006.818/7995	8007.775/7995	8009.766/7995
t_0 [HJD$'$]	7654.235 ± 0.192	7654.229 ± 0.192	7655.221 ± 0.175	7655.137 ± 0.177	7655.258 ± 0.177	7655.195 ± 0.178
u_0	0.106 ± 0.009	0.105 ± 0.010	0.401 ± 0.023	0.397 ± 0.020	-0.397 ± 0.020	-0.398 ± 0.031
t_E [days]	209.677 ± 16.086	211.183 ± 18.672	62.803 ± 3.843	63.190 ± 3.114	59.885 ± 2.917	60.581 ± 5.596
s	0.929 ± 0.005	0.961 ± 0.006	0.801 ± 0.010	0.826 ± 0.009	0.802 ± 0.008	0.825 ± 0.014
q ($\times 10^{-4}$)	0.416 ± 0.066	0.443 ± 0.068	1.009 ± 0.141	1.258 ± 0.161	1.072 ± 0.140	1.334 ± 0.180
$\langle \log_{10} q \rangle$	-4.378 ± 0.068	-4.366 ± 0.068	-3.983 ± 0.057	-3.923 ± 0.058	-3.945 ± 0.052	-3.890 ± 0.060
α [rad]	4.332 ± 0.011	4.329 ± 0.011	4.401 ± 0.012	4.394 ± 0.012	-4.385 ± 0.012	-4.384 ± 0.012
$\rho_{*,\mathrm{limit}}$	< 0.003	< 0.003	< 0.007	< 0.009	< 0.007	< 0.009
$\pi_{\mathrm{E},N}$	$\cdots$	$\cdots$	0.075 ± 0.059	0.070 ± 0.060	0.095 ± 0.080	0.074 ± 0.084
$\pi_{\mathrm{E},E}$	$\cdots$	$\cdots$	0.455 ± 0.037	0.441 ± 0.034	0.465 ± 0.035	0.449 ± 0.048

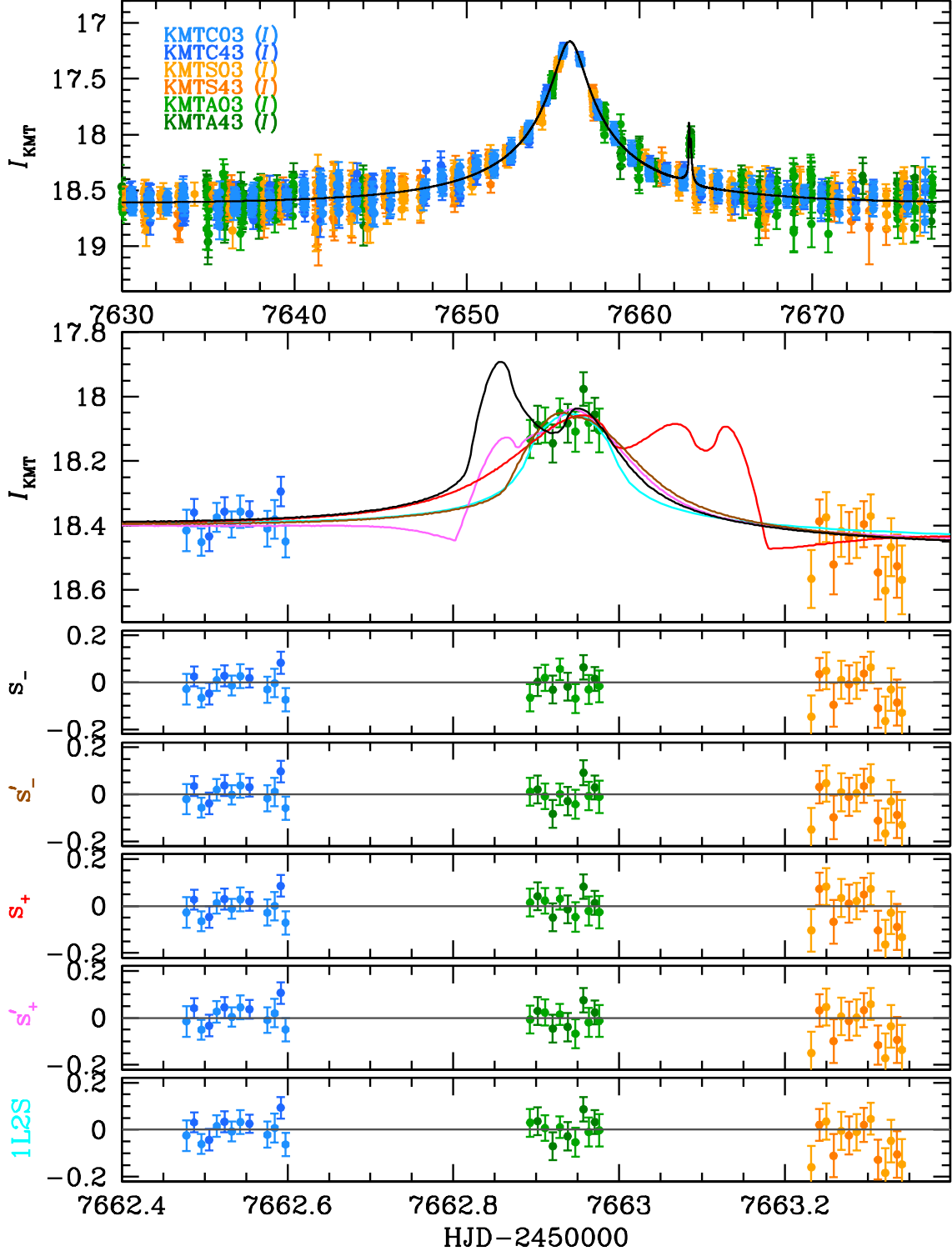NOTE— HJD$'$ = HJD $-$ 2450000.0.

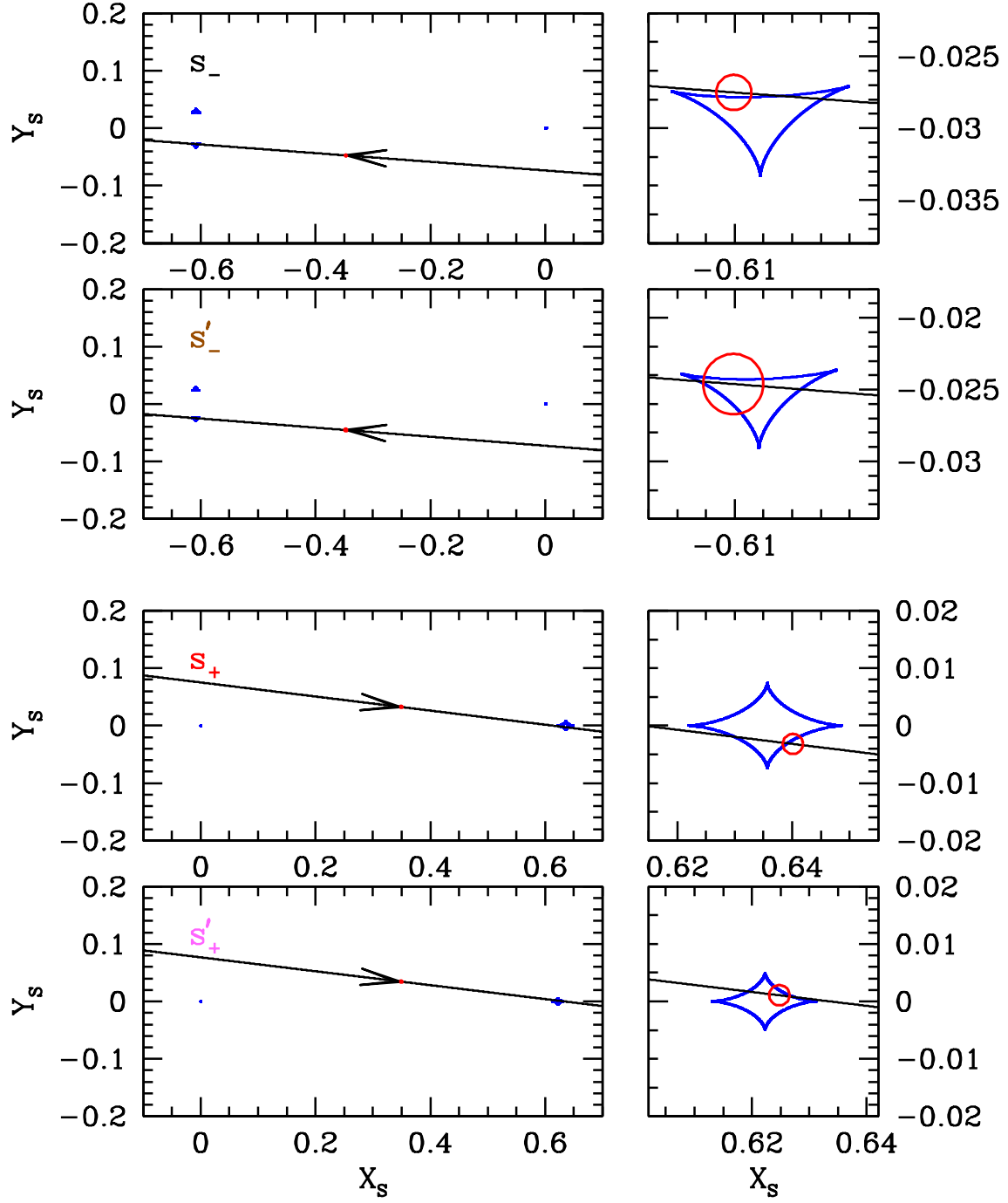**Figure 3.** Light curve of KMT-2016-BLG-0625 with degenerate models.

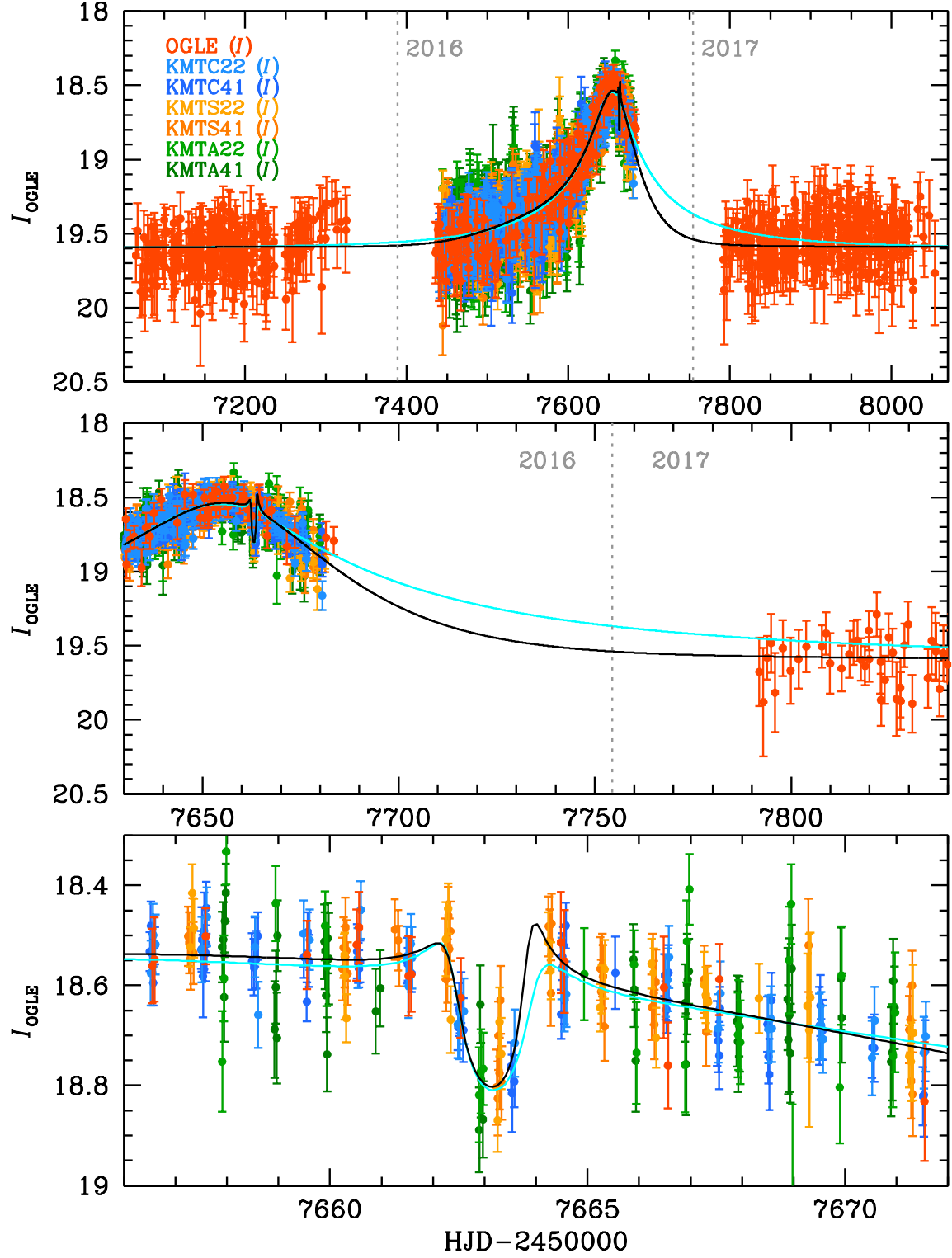**Figure 4.** Caustic geometries of KMT-2016-BLG-0625 for the 2L1S models.

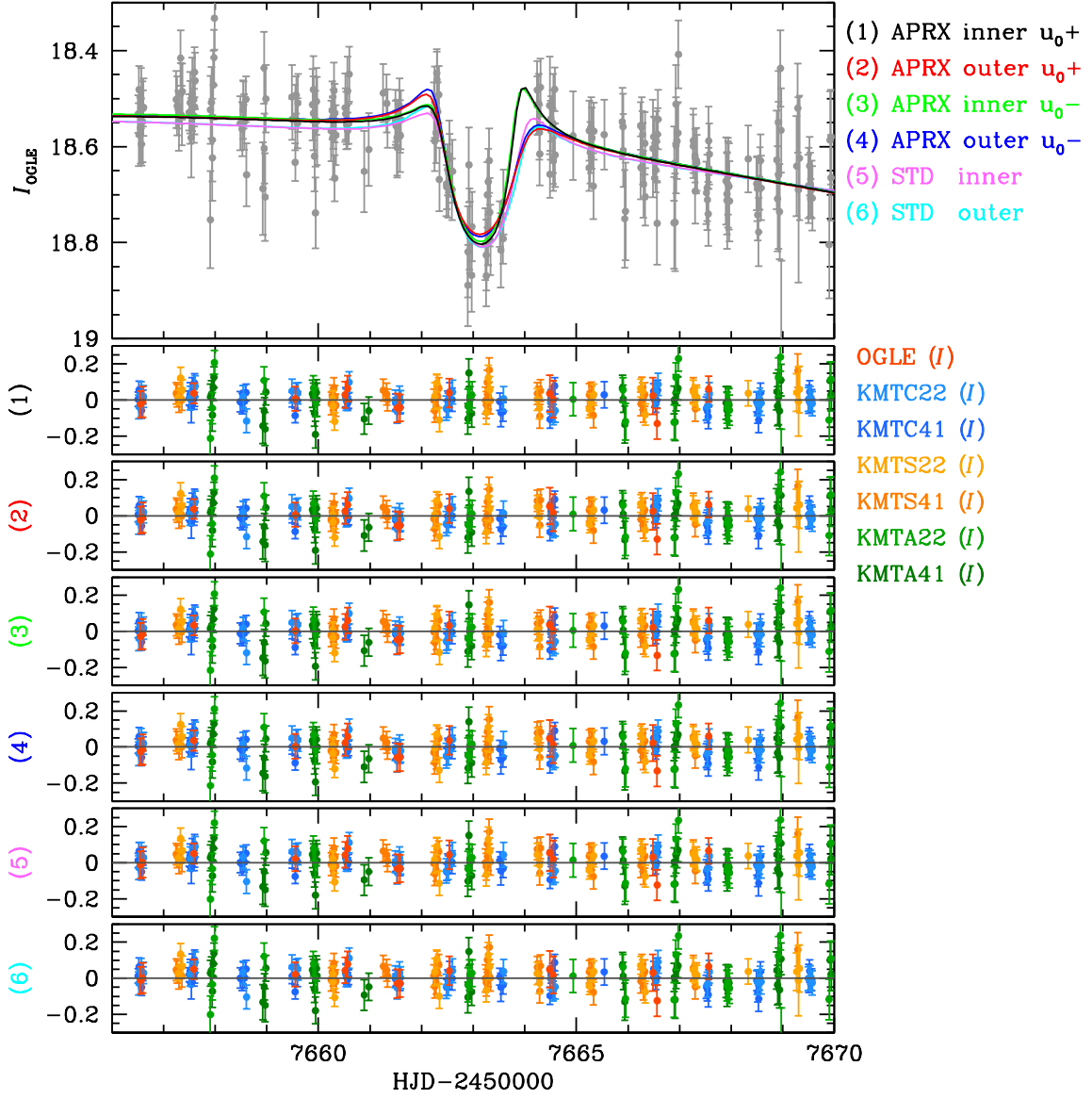**Figure 5.** Light curve of OGLE-2016-BLG-1850 with STD (cyan) and APRX (black) models.

Figure 6. Zoom-in of the anomaly part of OGLE-2016-BLG-1850 for comparing all models with their residuals.
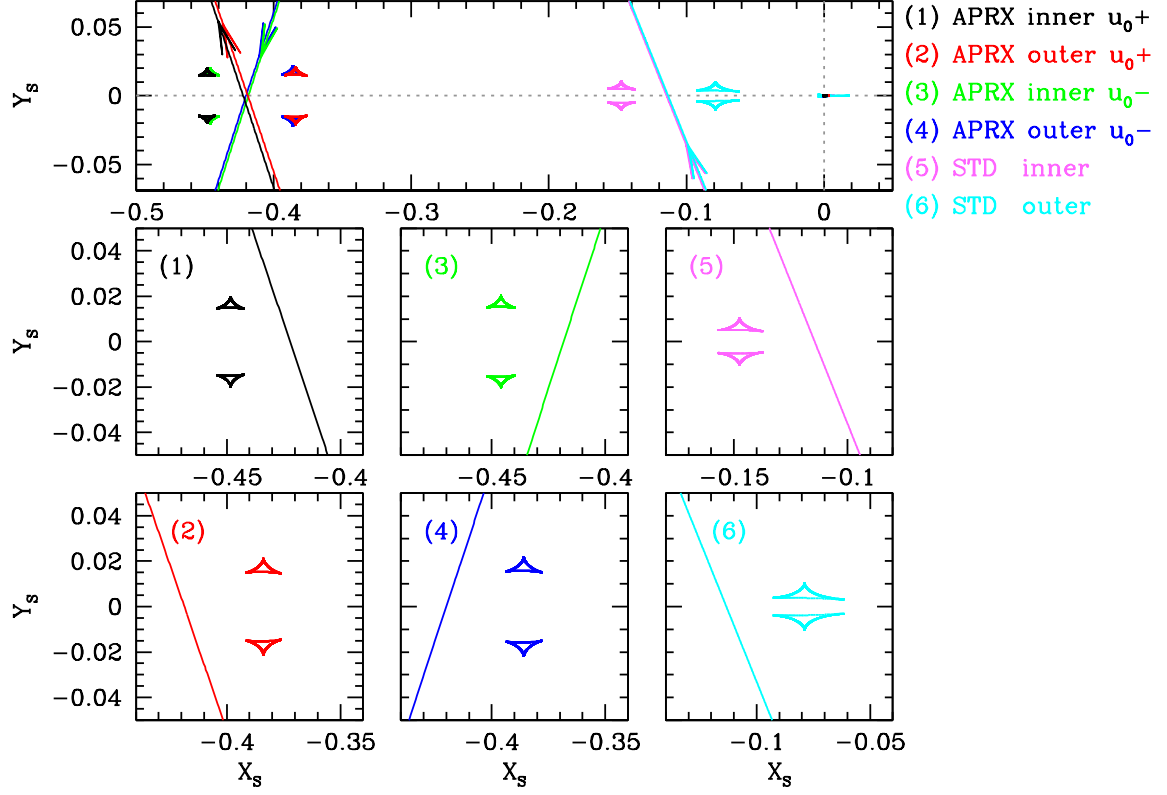
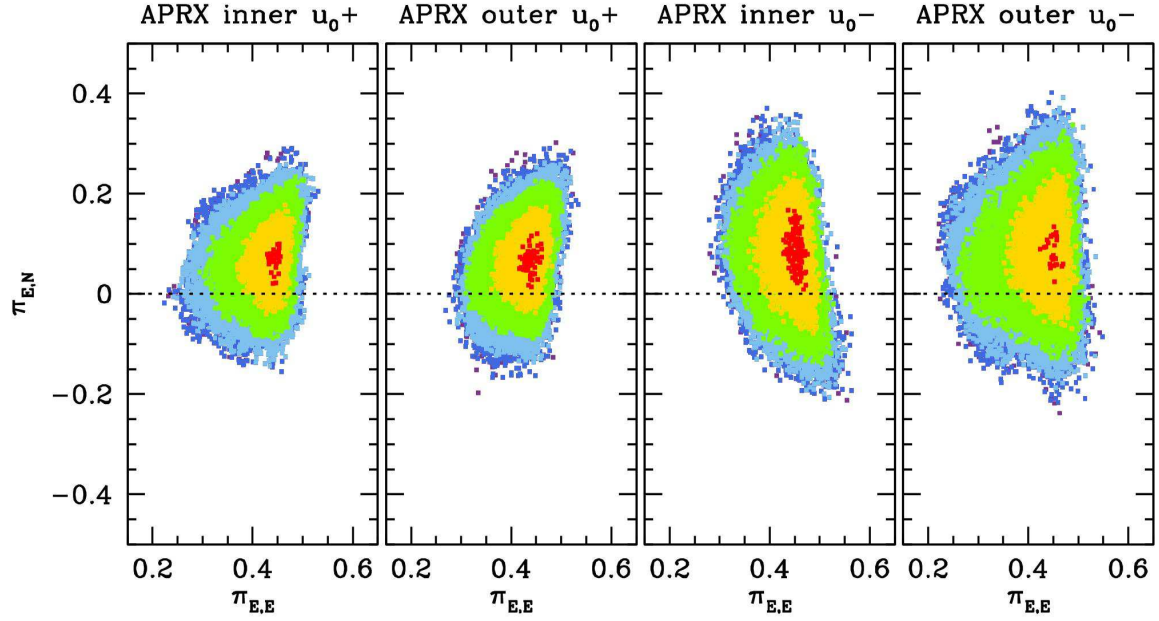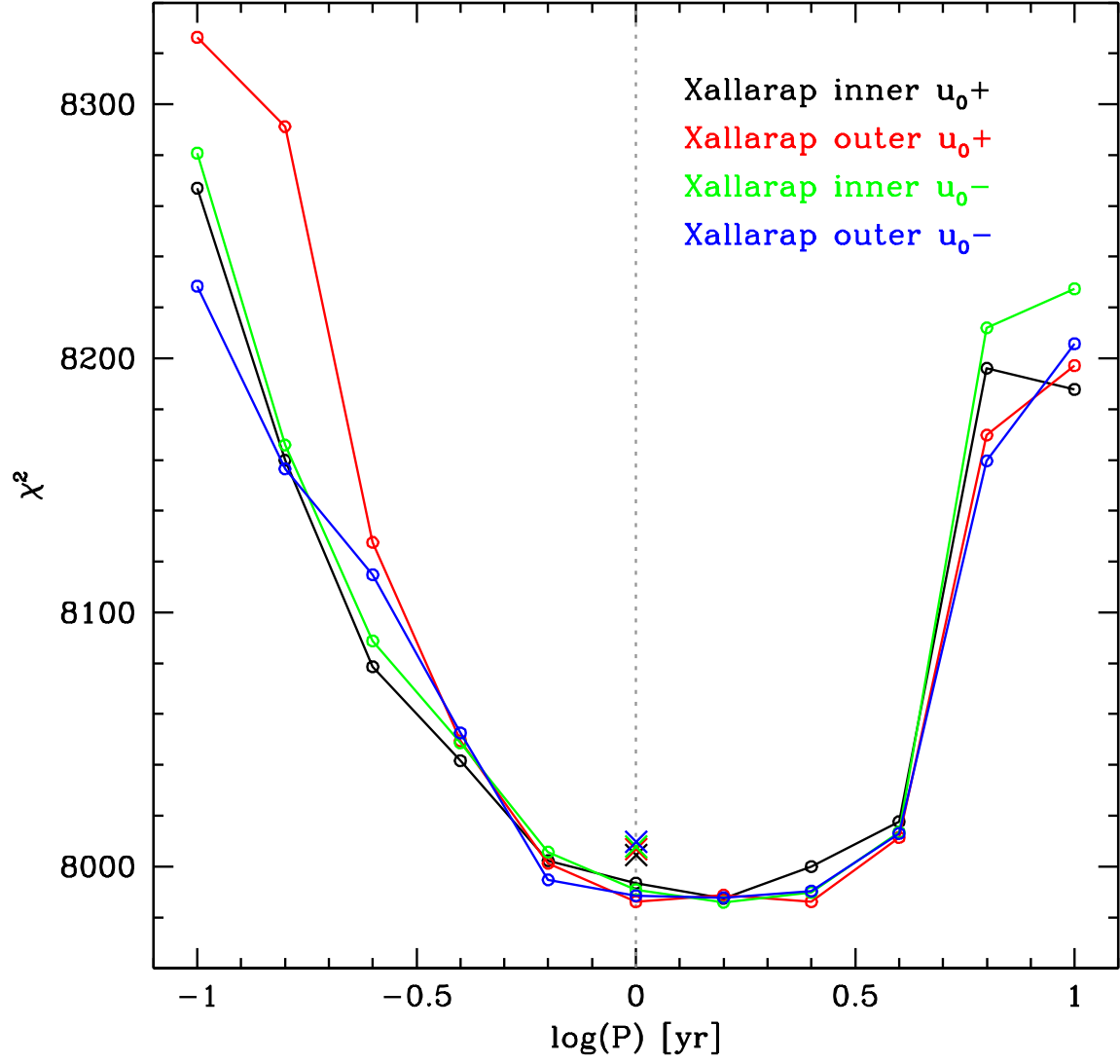**Figure 7.** Caustic geometries of OGLE-2016-BLG-1850.

Figure 8. The APRX distributions of OGLE-2016-BLG-1850.

Figure 9. $\log_{10}(P)$ and χ^2 plots of xallarap models of OGLE-2016-BLG-1850. The "X" marks indicate χ^2 of the APRX models.

Table 7. Model Parameters of KMT-2016-BLG-1751

Parameter	$\mathbf{s}_+$	$\mathbf{s}'_+$	$\mathbf{s}_-$	$\mathbf{s}'_-$	s''_-
$\chi^2/\mathrm{N}_{\mathrm{data}}$	**8995.960/8994**	**9004.487/8994**	**9001.658/8994**	**9004.738/8994**	9006.742/8994
t_0 [HJD$'$]	**7501.132 ± 0.016**	**7501.187 ± 0.021**	**7501.106 ± 0.017**	**7501.176 ± 0.019**	7501.214 ± 0.016
u_0	**0.113 ± 0.005**	**0.111 ± 0.005**	**0.107 ± 0.005**	**0.110 ± 0.005**	0.103 ± 0.006
t_{E} [days]	**9.625 ± 0.293**	**9.475 ± 0.292**	**9.997 ± 0.301**	**9.469 ± 0.284**	9.591 ± 0.298
s	**1.050 ± 0.014**	**1.027 ± 0.017**	**0.848 ± 0.011**	**0.873 ± 0.015**	0.950 ± 0.007
q ($\times 10^{-4}$)	**64.992 ± 4.479**	**39.995 ± 8.312**	**61.147 ± 3.556**	**38.161 ± 7.169**	7.207 ± 2.902
$\langle \log_{10} q \rangle$	**−2.200 ± 0.031**	**−2.447 ± 0.113**	**−2.212 ± 0.025**	**−2.485 ± 0.104**	−3.036 ± 0.130
α [rad]	**4.339 ± 0.022**	**4.470 ± 0.049**	**4.318 ± 0.021**	**4.467 ± 0.044**	4.643 ± 0.035
$\rho_{*,\mathrm{limit}}$	**< 0.019**	**< 0.020**	**< 0.021**	**< 0.020**	$\cdots$
ρ_*	$\cdots$	$\cdots$	$\cdots$	$\cdots$	0.019 ± 0.002

NOTE— HJD$'$ = HJD − 2450000.0.

Table 8. Model Parameters of KMT-2016-BLG-1855

Parameter	A: best–fit	A$'$: 3($\pi/2$)	B: 2($\pi/2$)	B$'$: 2($\pi/2$)
$\chi^2/\mathrm{N}_{\mathrm{data}}$	**7734.217/7735**	7749.828/7735	7758.514/7735	7757.884/7735
$\Delta\chi^2$ (full data)	$\cdots$	15.611	24.297	23.667
$\Delta\chi^2$ (HJD$'$ < 7600)	$\cdots$	13.196	8.055	8.821
t_0 [HJD$'$]	**7454.015 ± 0.080**	7455.619 ± 0.078	7453.981 ± 0.104	7455.694 ± 0.086
u_0	**0.041 ± 0.007**	0.040 ± 0.006	0.001 ± 0.001	−0.001 ± 0.001
t_{E} [days]	**94.156 ± 17.078**	103.244 ± 18.364	2889.644 ± 493.547	2924.318 ± 120.251
t'_{E} [days]	**14.424 ± 0.908**	15.331 ± 0.904	13.282 ± 0.984	13.321 ± 0.945
s	**3.798 ± 0.108**	3.780 ± 0.088	3.598 ± 0.132	3.708 ± 0.121
q	**42.614 ± 21.193**	45.352 ± 24.063	$(47.334 ± 11.658) \times 10^3$	$(48.189 ± 5.978) \times 10^3$
$\frac{1}{q}$	**0.023 ± 0.012**	0.022 ± 0.009	$(0.211 ± 0.419) \times 10^{-4}$	$(0.208 ± 0.042) \times 10^{-4}$
$\langle \log_{10} \frac{1}{q} \rangle$	**−1.605 ± 0.196**	−1.666 ± 0.173	−4.249 ± 0.248	−4.574 ± 0.068
α [rad]	**0.657 ± 0.012**	5.603 ± 0.016	3.812 ± 0.016	3.803 ± 0.015
$\rho_{*,\mathrm{limit}}$	**< 0.023**	< 0.024	< 0.002	< 0.0006

NOTE— HJD$'$ = HJD − 2450000.0.
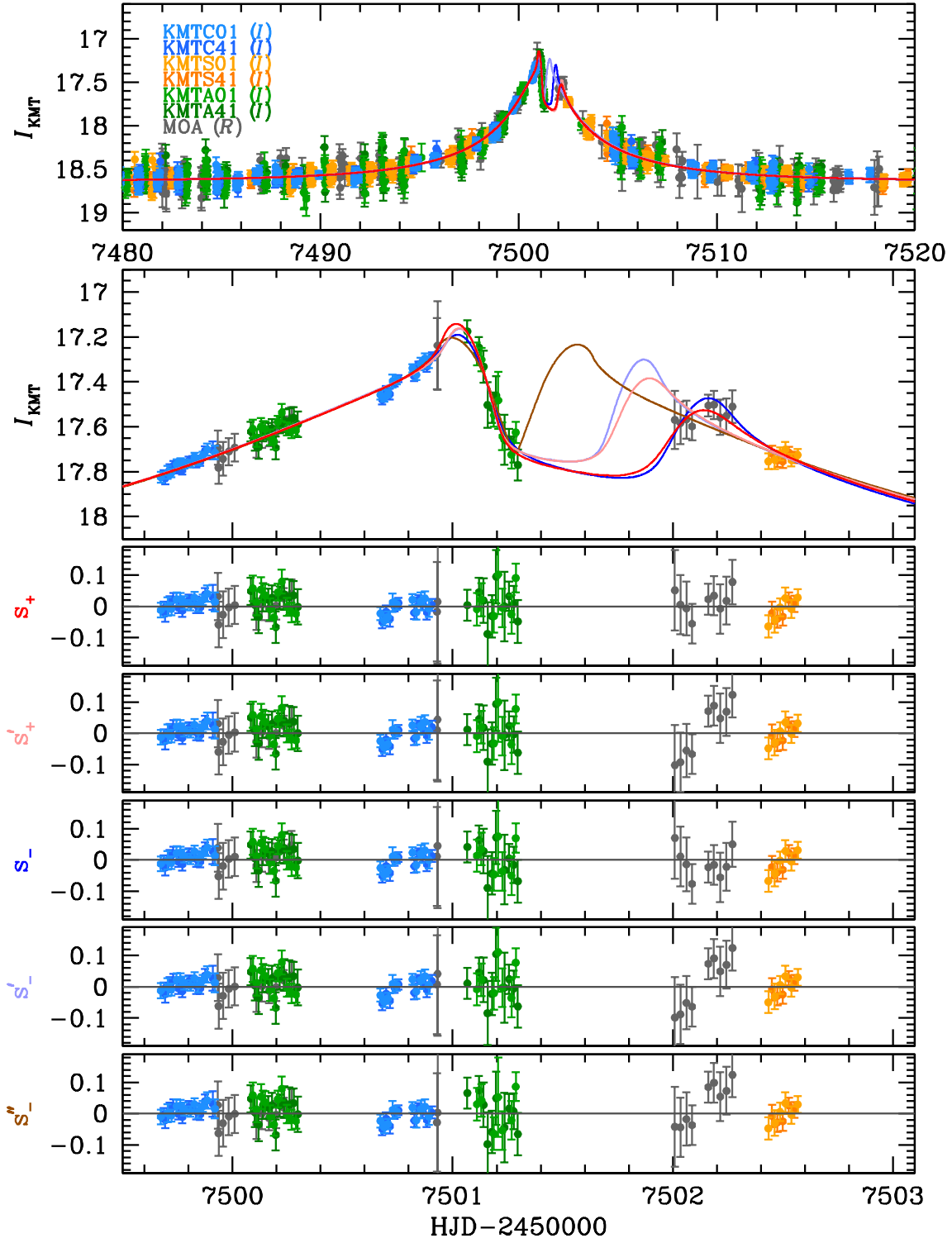
Figure 10. Light curve of KMT-2016-BLG-1751 with degenerate models.
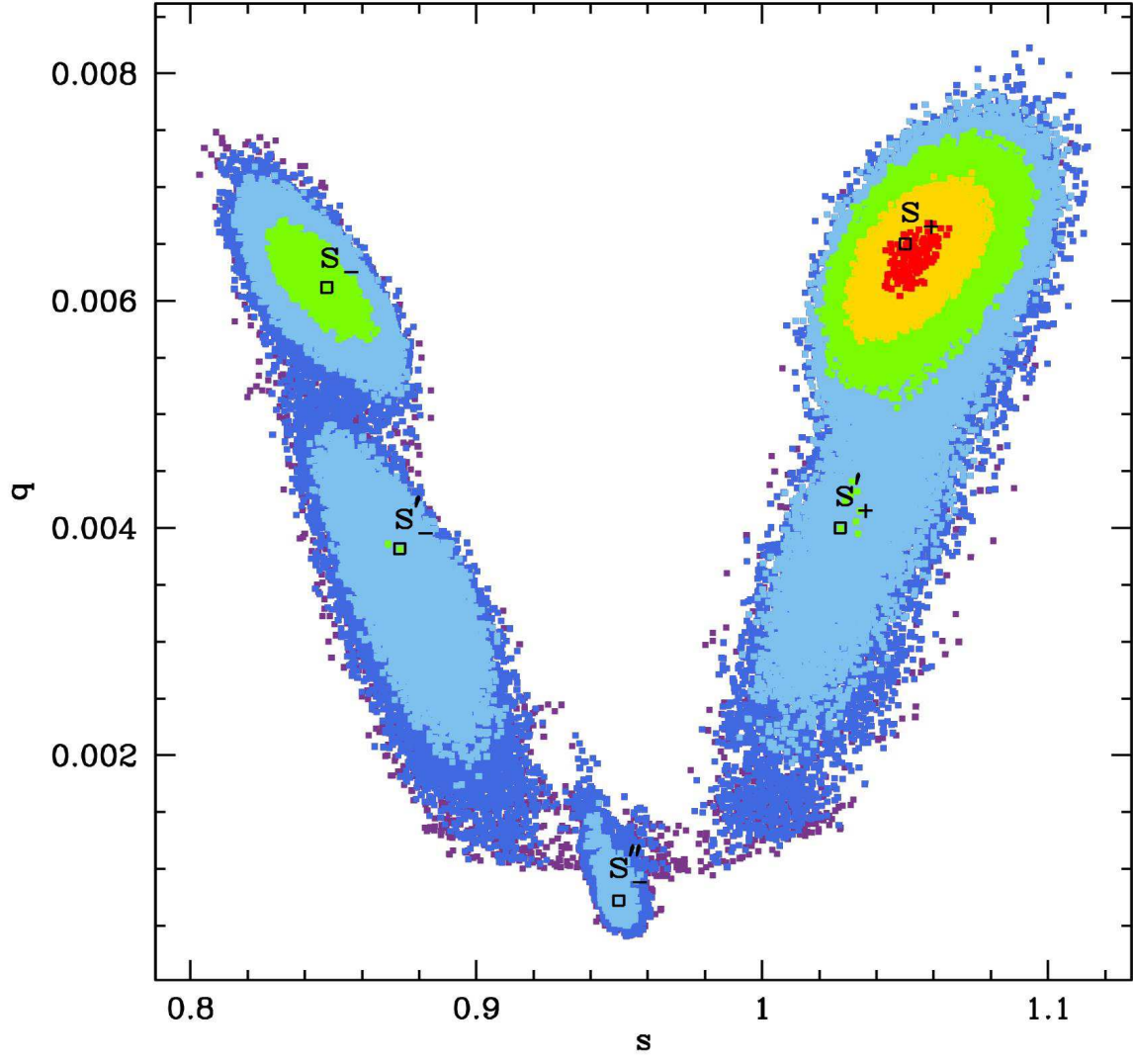
Figure 11. s–q parameter space of KMT-2016-BLG-1751 showing possible solutions.
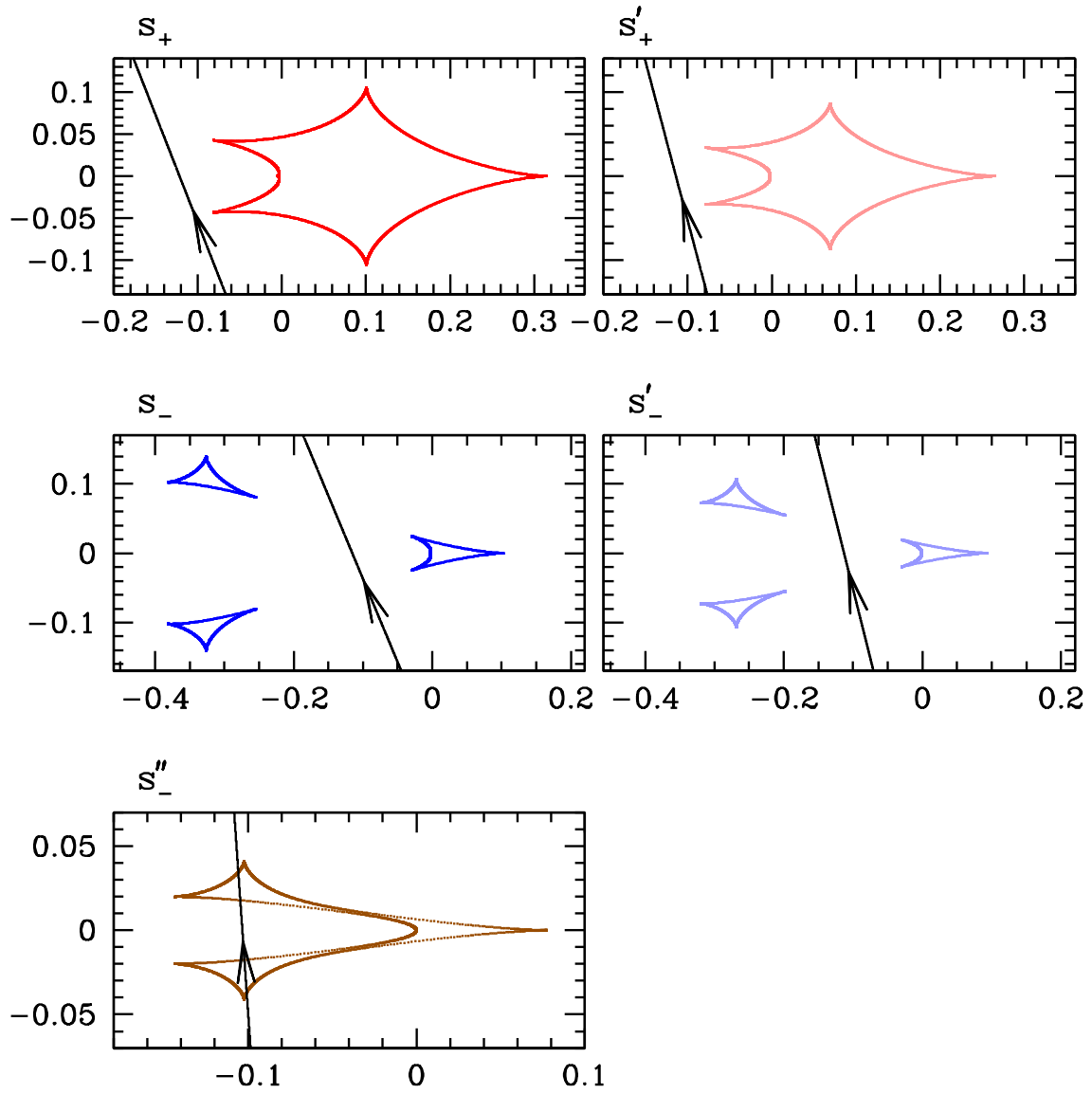
Figure 12. Caustic geometry of each solution of KMT-2016-BLG-1751. The color of caustic is identical to the color of the light curve shown in Figure 10.

Figure 13. Light curve of KMT-2016-BLG-1855 with the best–fit model.

Figure 14. Light curve of KMT-2016-BLG-1855 with the best–fit (A) and degenerate models of A′, B, and B′.
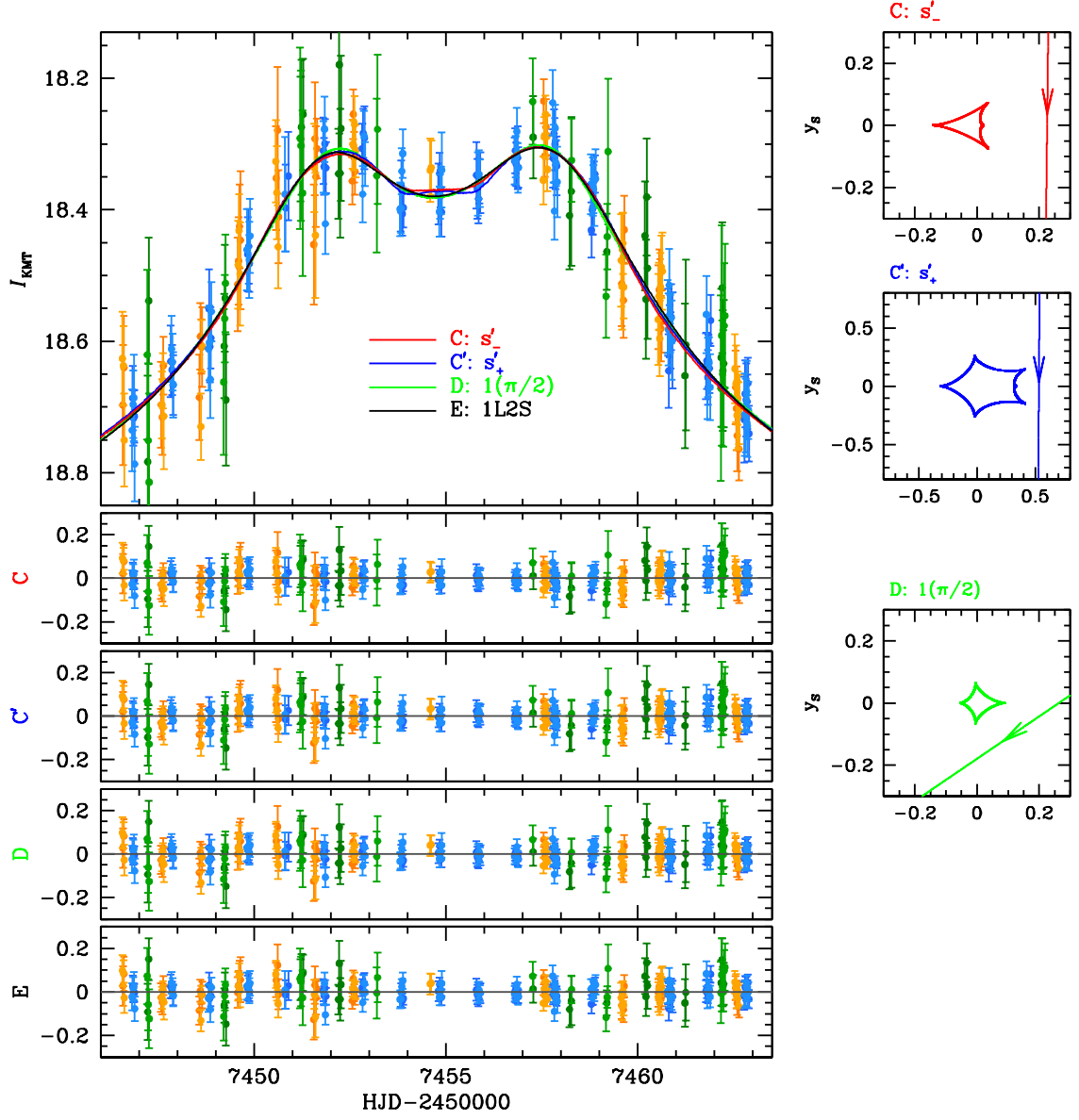
Figure 15. Light curve of KMT-2016-BLG-1855 with degenerate models of C, C′, D, and E.

Table 9. Model Parameters of KMT-2016-BLG-1855 (continue)

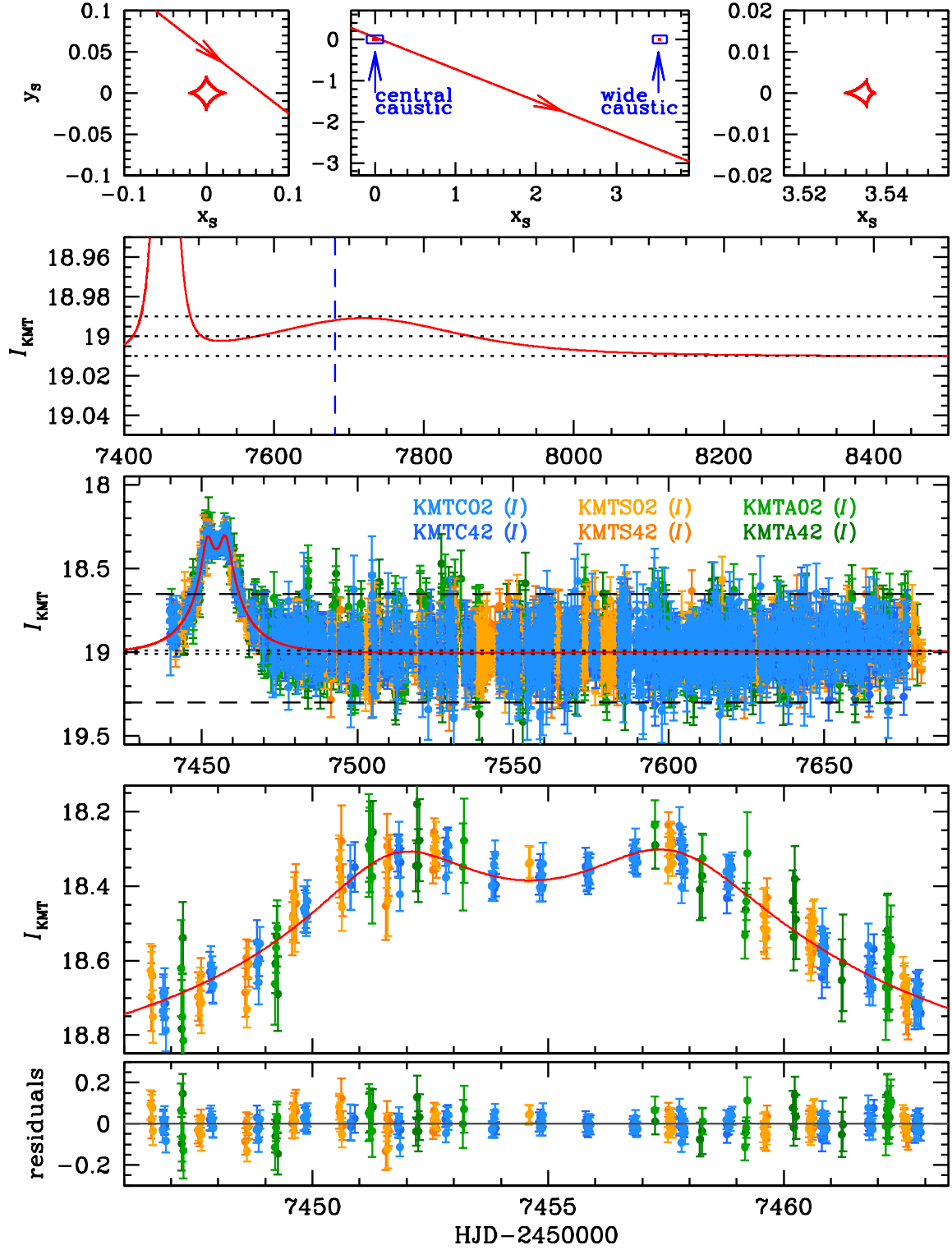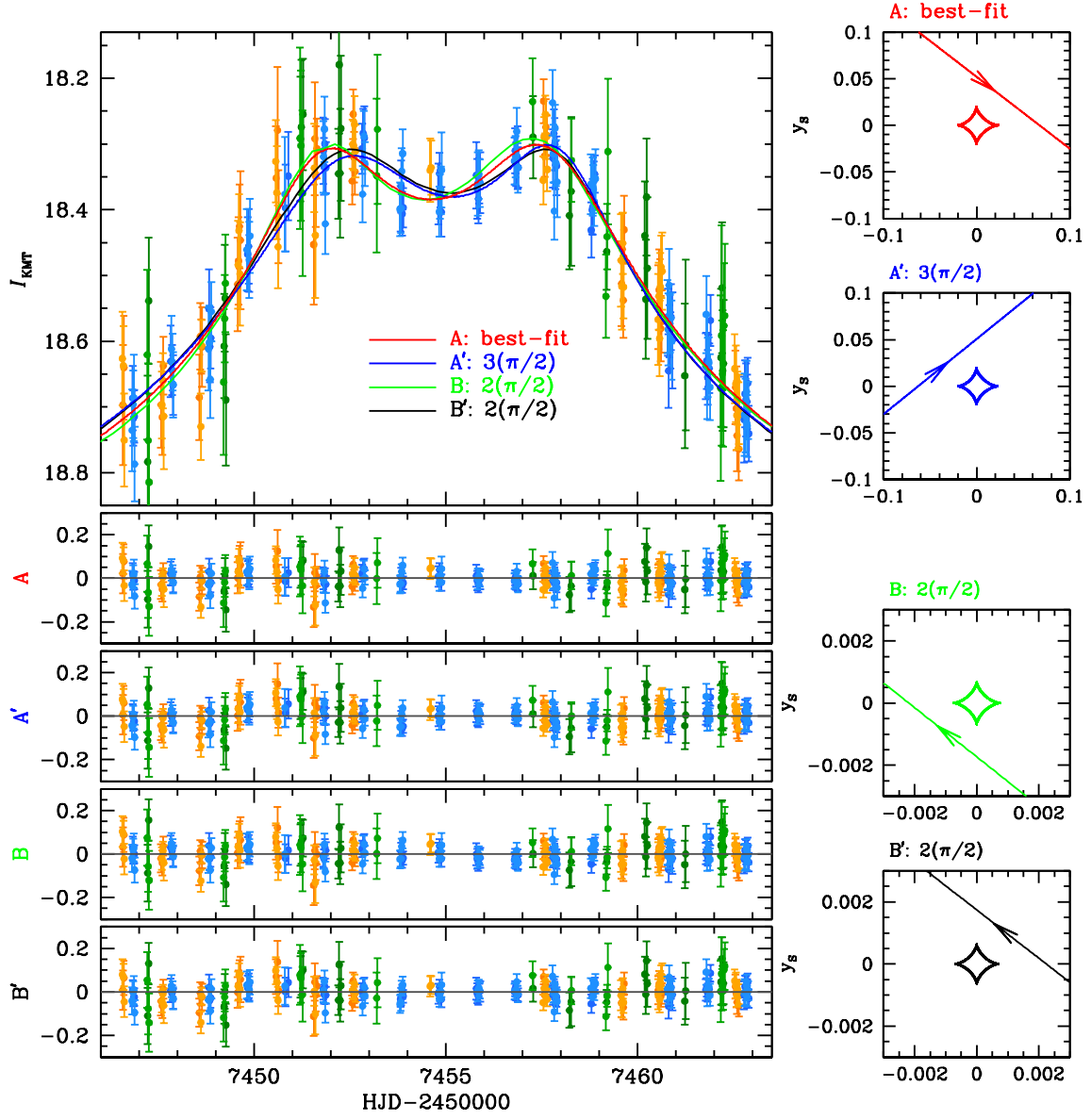| Parameter	C: s'_-	C': s'_+	D: $1(\pi/2)$	Parameter	E: 1L2S
$\chi^2/\mathrm{N_{data}}$	7751.738/7735	7750.972/7735	7755.555/7735	$\chi^2/\mathrm{N_{data}}$	7752.925/7735
$\Delta\chi^2$ (full data)	17.521	16.775	21.338	$\Delta\chi^2$ (full data)	18.708
$\Delta\chi^2$ (HJD$'<7600$)	2.269	1.414	5.727	$\Delta\chi^2$ (HJD$'<7600$)	3.060
t_0 [HJD$'$]	7454.864 ± 0.061	7454.893 ± 0.090	7455.816 ± 0.102	t_{0,S_1} [HJD$'$]	7451.870 ± 0.112
u_0	0.226 ± 0.049	0.531 ± 0.066	0.148 ± 0.024	u_{0,S_1}	0.124 ± 0.015
t_E [days]	15.382 ± 1.392	15.408 ± 1.392	24.015 ± 4.242	t_E [days]	17.409 ± 1.362
t'_E [days]	$\cdots$	$\cdots$	14.176 ± 1.999	t_{0,S_2} [HJD$'$]	7457.697 ± 0.106
s	0.687 ± 0.025	1.161 ± 0.042	3.392 ± 0.162	u_{0,S_1}	0.133 ± 0.018
q	18.911 ± 3.028	16.223 ± 2.143	2.870 ± 1.418	q_flux	1.146 ± 0.181
$\frac{1}{q}$	0.053 ± 0.006	0.062 ± 0.007	0.348 ± 0.215	$\cdots$	$\cdots$
$\langle\log_{10}\frac{1}{q}\rangle$	-1.328 ± 0.059	-1.229 ± 0.053	-0.389 ± 0.203	$\cdots$	$\cdots$
α [rad]	1.582 ± 0.013	1.578 ± 0.012	2.544 ± 0.014	$\cdots$	$\cdots$
$\rho_{*,\mathrm{limit}}$	<0.168	<0.178	<0.101	$\cdots$	$\cdots$

NOTE— HJD$'$ = HJD $- 2450000.0$.

Table 10. CMD analyses of Planetary Events

Event Case	$(V-I)_{\rm RGC}$	$(V-I)_{0,{\rm RGC}}$	$(V-I)_{\rm S}$	$(V-I)_{0,{\rm S}}$	$(V-I)_{\rm B}$	θ_*	$\theta_{\rm E}$	$\mu_{\rm rel}$
	$I_{\rm RGC}$	$I_{0,{\rm RGC}}$	$I_{\rm S}$	$I_{0,{\rm S}}$	$I_{\rm B}$	(μas)	(mas)	(mas yr^{-1})
OB161635								
s_-	2.763	1.060	2.441 ± 0.136	0.738 ± 0.145	2.503 ± 0.005	0.315 ± 0.050	> 0.085	> 1.49
	16.519	14.482	22.121 ± 0.015	20.084 ± 0.015	16.872 ± 0.001			
s_+	2.763	1.060	2.442 ± 0.137	0.739 ± 0.145	2.503 ± 0.005	0.311 ± 0.050	> 0.076	> 1.26
	16.519	14.482	22.153 ± 0.015	20.116 ± 0.015	16.872 ± 0.001			
MB16532								
s_-	2.313	1.060	2.952 ± 0.150	1.699 ± 0.158	2.135 ± 0.002	0.529 ± 0.035	0.113 ± 0.015	1.98 ± 0.26
	15.995	14.391	22.200 ± 0.008	20.596 ± 0.008	16.998 ± 0.001			
s_+	2.313	1.060	2.958 ± 0.150	1.705 ± 0.158	2.135 ± 0.002	0.534 ± 0.036	0.112 ± 0.016	1.99 ± 0.29
	15.995	14.391	22.188 ± 0.008	20.584 ± 0.008	16.997 ± 0.001			
KB160625								
s_-	1.892	1.060	1.427 ± 0.044	0.595 ± 0.066	1.584 ± 0.005	0.364 ± 0.025	0.297 ± 0.029	9.44 ± 0.93
	15.331	14.335	20.412 ± 0.010	19.416 ± 0.010	17.363 ± 0.001			
s'_-	1.892	1.060	1.429 ± 0.044	0.597 ± 0.066	1.583 ± 0.005	0.363 ± 0.025	0.173 ± 0.017	5.46 ± 0.54
	15.331	14.335	20.423 ± 0.010	19.427 ± 0.010	17.362 ± 0.001			
s_+	1.892	1.060	1.429 ± 0.043	0.597 ± 0.066	1.584 ± 0.005	0.368 ± 0.026	0.210 ± 0.021	6.78 ± 0.67
	15.331	14.335	20.390 ± 0.010	19.394 ± 0.010	17.364 ± 0.001			
s'_+	1.892	1.060	1.429 ± 0.043	0.597 ± 0.066	1.584 ± 0.005	0.372 ± 0.026	0.210 ± 0.021	6.85 ± 0.68
	15.331	14.335	20.371 ± 0.010	19.375 ± 0.010	17.366 ± 0.001			
OB161850								
APRX inner u_0+	2.552	1.060	2.106 ± 0.048	0.614 ± 0.069	1.738 ± 0.031	0.880 ± 0.064	> 0.126	> 0.73
	16.502	14.558	19.488 ± 0.007	17.544 ± 0.007	18.868 ± 0.007			
APRX outer u_0+	2.552	1.060	2.108 ± 0.048	0.616 ± 0.069	1.740 ± 0.030	0.874 ± 0.064	> 0.097	> 0.56
	16.502	14.558	19.508 ± 0.007	17.564 ± 0.007	18.854 ± 0.006			
APRX inner u_0-	2.552	1.060	2.106 ± 0.048	0.614 ± 0.069	1.743 ± 0.030	0.871 ± 0.064	> 0.124	> 0.76
	16.502	14.558	19.510 ± 0.007	17.565 ± 0.007	18.848 ± 0.006			
APRX outer u_0-	2.552	1.060	2.108 ± 0.048	0.616 ± 0.069	1.743 ± 0.030	0.873 ± 0.064	> 0.097	> 0.58

Table 10 *continued on next page*

Table 10 *(continued)*

Event Case	$(V-I)_{\rm RGC}$ $I_{\rm RGC}$	$(V-I)_{0,\rm RGC}$ $I_{0,\rm RGC}$	$(V-I)_{\rm S}$ $I_{\rm S}$	$(V-I)_{0,\rm S}$ $I_{0,\rm S}$	$(V-I)_{\rm B}$ $I_{\rm B}$	θ_* $(\mu{\rm as})$	$\theta_{\rm E}$ (mas)	$\mu_{\rm rel}$ $({\rm mas\,yr^{-1}})$
	16.502	14.558	9.511 ± 0.007	17.566 ± 0.007	18.847 ± 0.006			
KB161751								
s_+	2.664	1.060	2.083 ± 0.056	0.479 ± 0.075	3.034 ± 0.068	0.543 ± 0.038	0.039 ± 0.010	> 1.06
	16.657	14.548	20.407 ± 0.007	18.299 ± 0.007	19.431 ± 0.004			
s'_+	2.664	1.060	2.083 ± 0.057	0.479 ± 0.076	3.059 ± 0.073	0.554 ± 0.039	0.040 ± 0.011	> 1.06
	16.657	14.548	20.366 ± 0.007	18.258 ± 0.007	19.448 ± 0.004			
s_-	2.664	1.060	2.084 ± 0.057	0.480 ± 0.076	2.998 ± 0.062	0.527 ± 0.037	0.041 ± 0.014	> 0.94
	16.657	14.548	20.477 ± 0.007	18.368 ± 0.007	19.404 ± 0.004			
s'_-	2.664	1.060	2.084 ± 0.057	0.480 ± 0.076	3.052 ± 0.072	0.551 ± 0.039	0.044 ± 0.015	> 1.05
	16.657	14.548	20.375 ± 0.007	18.267 ± 0.007	19.444 ± 0.004			
s''_-	2.664	1.060	2.084 ± 0.057	0.480 ± 0.075	3.047 ± 0.071	0.549 ± 0.039	0.029 ± 0.004	1.09 ± 0.17
	16.657	14.548	20.387 ± 0.007	18.279 ± 0.007	19.439 ± 0.004			

NOTE—We use the abbreviation for event names, e.g., OGLE-2016-BLG-1635 is abbreviated as OB161635.

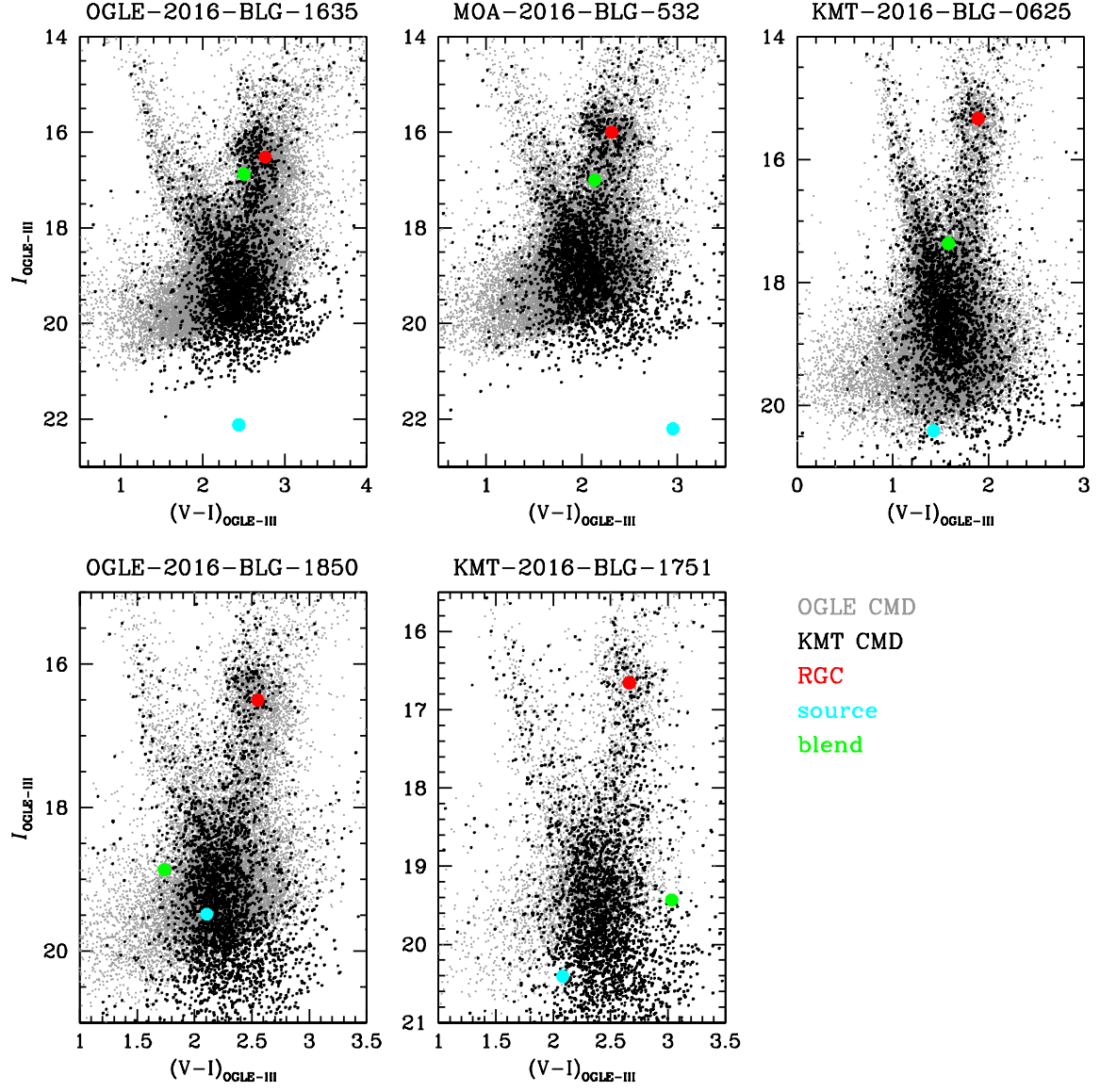**Figure 16.** Color–magnitude diagrams (CMD) of five planetary events.

Table 11. Lens Properties of Planetary Events

Event	Constraints	Case	$M_{\rm host}$ ($M_\odot$)	$M_{\rm planet}$ ($M_{\rm J}$ / $M_{\rm N}$ / $M_\oplus$)	$D_{\rm L}$ (kpc)	$a_\perp$ (au)	$\mu_{\rm rel}$ (mas yr^{-1})	Gal. Mod.	χ^2
OB161635	$t_{\rm E} + \rho_*$	s_-	$0.43^{+0.33}_{-0.27}$	$11.49^{+8.91}_{-7.25}\,M_{\rm J}$	$6.62^{+1.15}_{-1.68}$	$1.31^{+0.50}_{-0.47}$	$6.32^{+2.89}_{-2.25}$	1.000	1.000
		s_+	$0.44^{+0.33}_{-0.27}$	$11.48^{+8.57}_{-7.28}\,M_{\rm J}$	$6.60^{+1.15}_{-1.71}$	$3.82^{+1.43}_{-1.37}$	$6.14^{+2.82}_{-2.20}$	0.723	0.021
Adopted			0.43 ± 0.29	$11.49 \pm 7.96\,M_{\rm J}$	6.62 ± 1.39	1.34 ± 0.47	6.32 ± 2.53		
MB16532	$t_{\rm E} + \theta_{\rm E}$	s_-	$0.09^{+0.14}_{-0.05}$	$7.18^{+11.35}_{-3.90}\,M_{\rm N}$	$7.38^{+0.97}_{-1.02}$	$0.56^{+0.10}_{-0.10}$	$2.10^{+0.30}_{-0.28}$	1.000	0.520
		s_+	$0.09^{+0.15}_{-0.05}$	$7.23^{+11.46}_{-4.05}\,M_{\rm N}$	$7.37^{+0.97}_{-1.02}$	$1.36^{+0.26}_{-0.25}$	$2.14^{+0.34}_{-0.31}$	0.997	1.000
Adopted			0.09 ± 0.07	$7.21 \pm 5.73\,M_{\rm N}$	7.37 ± 0.74	1.09 ± 0.17	2.13 ± 0.23		
KB160625	$t_{\rm E} + \theta_{\rm E}$	s_-	$0.30^{+0.30}_{-0.16}$	$1.36^{+1.90}_{-0.73}\,M_{\rm N}$	$6.14^{+0.95}_{-1.28}$	$1.31^{+0.24}_{-0.28}$	$9.25^{+0.98}_{-0.97}$	1.000	1.000
		s'_-	$0.15^{+0.21}_{-0.08}$	$8.98^{+17.84}_{-5.20}\,M_\oplus$	$6.68^{+0.94}_{-1.04}$	$0.86^{+0.15}_{-0.15}$	$5.53^{+0.58}_{-0.57}$	0.365	0.603
		s_+	$0.19^{+0.26}_{-0.10}$	$4.68^{+6.42}_{-2.92}\,M_\oplus$	$6.52^{+0.94}_{-1.11}$	$1.85^{+0.33}_{-0.35}$	$6.80^{+0.72}_{-0.70}$	0.556	0.612
		s'_+	$0.19^{+0.26}_{-0.10}$	$2.03^{+3.53}_{-1.06}\,M_\oplus$	$6.51^{+0.94}_{-1.11}$	$1.84^{+0.33}_{-0.34}$	$6.85^{+0.71}_{-0.69}$	0.574	0.193
Adopted			0.25 ± 0.14	$0.94 \pm 0.80\,M_{\rm N}$	6.31 ± 0.71	1.40 ± 0.17	8.10 ± 0.61		
OB161850	$t_{\rm E} + \rho_* + \boldsymbol{\pi}_{\rm E}$	APRX inner u_0+	$0.26^{+0.20}_{-0.12}$	$8.85^{+7.03}_{-4.19}\,M_\oplus$	$2.12^{+1.17}_{-0.80}$	$1.46^{+0.22}_{-0.26}$	$5.09^{+3.94}_{-2.30}$	0.905	1.000
		APRX outer u_0+	$0.26^{+0.20}_{-0.12}$	$10.73^{+8.59}_{-5.36}\,M_\oplus$	$2.14^{+1.19}_{-0.82}$	$1.49^{+0.22}_{-0.27}$	$4.95^{+3.94}_{-2.28}$	0.914	0.306
		APRX inner u_0-	$0.24^{+0.20}_{-0.11}$	$8.70^{+7.20}_{-3.98}\,M_\oplus$	$2.09^{+1.13}_{-0.79}$	$1.41^{+0.20}_{-0.24}$	$5.17^{+4.09}_{-2.32}$	0.923	0.190
		APRX outer u_0-	$0.26^{+0.20}_{-0.12}$	$11.47^{+9.05}_{-5.70}\,M_\oplus$	$2.22^{+1.19}_{-0.83}$	$1.50^{+0.26}_{-0.28}$	$5.17^{+3.94}_{-2.37}$	1.000	0.070
Adopted			0.26 ± 0.11	$9.33 \pm 3.88\,M_\oplus$	2.12 ± 0.67	1.46 ± 0.16	5.07 ± 2.11		
KB161751	$t_{\rm E} + \rho_*$	s_+	$0.18^{+0.28}_{-0.11}$	$1.21^{+1.88}_{-0.76}\,M_{\rm J}$	$7.05^{+1.16}_{-1.38}$	$1.40^{+0.60}_{-0.49}$	$7.49^{+3.46}_{-2.70}$	0.835	1.000
		s'_+	$0.17^{+0.27}_{-0.11}$	$0.73^{+1.14}_{-0.48}\,M_{\rm J}$	$7.05^{+1.16}_{-1.38}$	$1.36^{+0.58}_{-0.48}$	$7.51^{+3.48}_{-2.71}$	0.719	0.014
		s_-	$0.18^{+0.28}_{-0.12}$	$1.18^{+1.82}_{-0.74}\,M_{\rm J}$	$7.05^{+1.15}_{-1.38}$	$1.16^{+0.50}_{-0.41}$	$7.37^{+3.42}_{-2.66}$	1.000	0.058
		s'_-	$0.17^{+0.27}_{-0.11}$	$0.69^{+1.08}_{-0.48}\,M_{\rm J}$	$7.05^{+1.16}_{-1.37}$	$1.15^{+0.49}_{-0.41}$	$7.49^{+3.47}_{-2.70}$	0.696	0.012
Adopted			0.18 ± 0.18	$1.20 \pm 1.21\,M_{\rm J}$	7.05 ± 1.17	1.39 ± 0.50	7.49 ± 2.83		

NOTE—For the planet mass, we present the value in Jupiter ($M_{\rm J}$), Neptune ($M_{\rm N}$), or Earth ($M_\oplus$) masses as appropriate.

**Table 12.** Planetary events discovered on KMTNet prime fields in 2016

Event Name	KMT Name	$\log_{10}(q)$	s	Degeneracy	Reference
OB160007	KB161991	-5.17	2.83		Zang et al. (in prep.)
OB161195*	KB160372	-4.34	0.99	c/w, ecliptic	Gould et al. (2023)
OB161850	KB161307	-4.00	0.80	i/o, ecliptic	This work
MB16319	KB161816	-2.41	0.82	i/o	Han et al. (2018)
MB16532	KB160506	-2.39	0.65	c/w	This work
KB161836		-2.35	1.30	c/w, ecliptic	Yang et al. (2020)
MB16227	KB160622	-2.03	0.93		Koshimoto et al. (2017)
OB160596	KB161677	-1.93	1.08		Mróz et al. (2017)
KB162605		-1.92	0.94		Ryu et al. (2021)
OB161190	KB160113	-1.84	0.60	ecliptic	Ryu et al. (2018)
OB161635	KB160269	-1.59	0.59	c/w	This work
KB160625		-3.63	0.74	c/w	This work
OB160613**	KB160017	-2.26	1.06	c/w	Han et al. (2017)
KB161751		-2.19	1.05	c/w	This work
KB161855***		-1.61	3.80	c/w, α, offset, 1L2S	This work
KB160212		-1.43	0.83	c/w	Hwang et al. (2018)
KB161820		-0.95	1.40		Jung et al. (2018)
KB162142***		-0.69	0.97	c/w	Jung et al. (2018)

NOTE— *For OB161195, the properties of this planetary system was reported by Shvartzvald et al. (2017) and Bond et al. (2017). However, we adopt $\log_{10}(q)$ and s values from Gould et al. (2023), which re-analyze the event and measure a more precise mass ratio. **For OB160613, the event was caused by a lens system consisting of a planet and binary host stars. ***For KB161855 and KB162142, these are planet candidates. In the column of "Degeneracy", we present the type of degeneracies for the solutions: "c/w", "i/o", "ecliptic", "offset", "α", and "1L2S" indicate the close/wide degeneracy, inner/outer degeneracy, ecliptic degeneracy of the microlens–parallax effect, offset–degeneracy, α–degeneracy (see Section 3.7), and 2L1S/1L2S degeneracy, respectively.
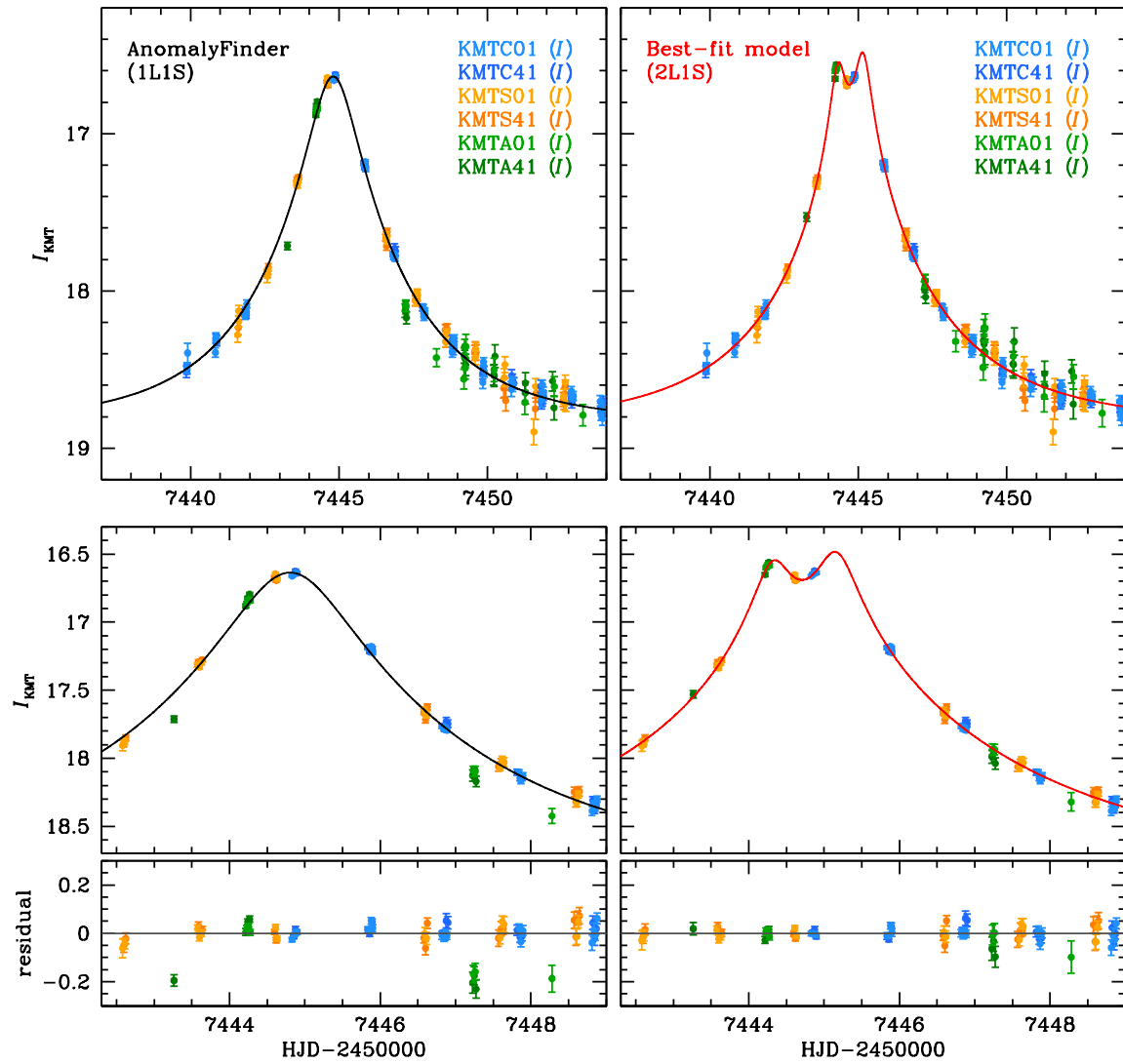
Figure 17. Comparison of light curves between AnomalyFinder (1L1S) and the best–fit (2L1S) for OGLE-2016-BLG-0185. Note that the data sets shown in this figure are produced by the KMTNet pipeline, which is actually used for the AnomalyFinder process.